American Mineralogist, Volume 111, pages 376–393, 2026

Microstructural and chemical responses of lunar pyroxene to shock shearing under low-to-moderate shock conditions

JIAWEI ZHAO[1,†], XIANG ZHANG[2], YUQING CHANG[2], AXEL WITTMANN[3], ZHIYONG XIAO[4], XIANG WU[1], CHANG XU[1], YUQI QIAN[1], QI HE[1], SIYUAN ZHAO[1], KENAN CAO[1], HAIPENG SONG[1], CHENG QIAN[1], WENTAO HU[2], BIJI LUO[1], ZHENBING SHE[1], FABIN PAN[1], AND LONG XIAO[1,5,*]

[1]State Key Laboratory of Geological Processes and Mineral Resources, Planetary Science Institute, School of Earth Sciences, China University of Geosciences, Wuhan 430074, China
[2]Center for High Pressure Science (CHiPS), State Key Laboratory of Metastable Materials Science and Technology, Yanshan University, Qinhuangdao, Hebei 066000, China
[3]Eyring Materials Center, Arizona State University, Tempe, Arizona 85287, U.S.A.
[4]Planetary Environmental and Astrobiological Research Laboratory (PEARL), School of Atmospheric Sciences, Sun Yat-sen University, Zhuhai, Guangdong, China
[5]State Key Laboratory of Lunar and Planetary Sciences, Space Science Institute, Macau University of Science and Technology, Macau, China

ABSTRACT

Pyroxene is a primary constituent mineral in basaltic lunar regolith. These minerals form through the cooling and crystallization of lunar basaltic magma and are subsequently altered by impact events. Thus, pyroxene can serve as a significant indicator for interpreting lunar magmatic processes and impact phenomena. For lunar samples that are mostly mafic and frequently shocked to various degrees, deciphering the effect of shock on pyroxene is necessary for a better understanding of the primary magmatic processes. However, previous studies have neglected to investigate the impact metamorphism of pyroxene in lunar regolith and the potential compositional changes that may result from such impacts. Lunar regolith samples returned by the Chang'E-5 (CE-5) mission are reworked from a monolithic mafic protolith with well-constrained compositions and record strong to mild shock effects that are widespread in the samples. The returned samples provide an excellent chance to distinguish the signatures of impact processes from magmatic activities. Here we report microstructural and compositional variations in a shocked pyroxene within a basaltic clast from CE-5 lunar regolith, which were analyzed by Raman spectroscopy, analytical scanning electron microscopy, electron probe microanalysis, and scanning transmission electron microscopy. The shock microstructures are characterized by the glide system of dislocation [001](100), pigeonite formation induced by shock-related deformations, and solid-melt partitioning and localized frictional melting at grain boundaries or within pyroxene. Combined with the occurrence of shock twins in ilmenite adjacent to the shock melt vein, these shock phenomena are approximately indicative of low-to-moderate shock pressure (9–17 GPa). Most parts of the pyroxene have abnormal Raman peaks at ~822 cm^{-1}, suggesting the substitution of Si^{4+} by Al^{3+} in the tetrahedral site of this shocked pyroxene structure, and this characteristic is recognized as a shock indicator. Evidence from the morphology and elemental distribution of pigeonite within host augite suggests that the Si-Al substitution is consistent with the pigeonite formation, which is triggered or modified by shock-induced deformations and local frictional melting under the fast shear stress. The multiple trends of composition evolution in this single shocked pyroxene reflect sequential processes of magma crystallization, shock-related exsolution, and frictional melting. Our findings indicate that shock effects in pyroxene under low-to-moderate shock conditions can induce changes in composition and structure, and may obscure the evidence of magmatic evolution in pyroxene.

Keywords: Shocked pyroxene, pigeonite formation, frictional melting, plastic deformations, CE-5 lunar sample

INTRODUCTION

Pyroxene is a major rock-forming mineral in the crust and mantle of both terrestrial bodies (e.g., Earth, Moon, Mars, and others) and small bodies in the Solar System (Papike et al. 2005). Its widespread presence serves as an important indicator for magmatic processes, including magma source, transport, and crystallization (Bence and Papike 1972; Presnall and Gasparik 1990). Thus, pyroxene acts as an important recorder for the crystallization history of basaltic magmas, reflecting changes in mineralogy, chemistry, and thermodynamic properties such as temperature, pressure, magma composition, and oxygen fugacity during crystallization (Bence and Papike 1972; Wu et al. 2024).

---

* Corresponding author E-mail: longxiao@cug.edu.cn
† Orcid https://orcid.org/0000-0003-4569-0722

0003-004X/26/0003–376$05.00/DOI: https://doi.org/10.2138/am-2025-9877

Pyroxene can also preserve signatures of extreme impact conditions, such as extreme pressure and temperature conditions, as well as high strain rates, through microstructural transformations (Ringwood and Major 1966; Leroux 2001). Deformation features in shocked pyroxene, such as dislocation glide systems and twinning, have been well documented in shocked extraterrestrial materials, including chondrites (Ashworth 1980; Langenhorst et al. 1995) and martian meteorites (Müller 1993; Leroux et al. 2004, 2016; Daly et al. 2019). Additionally, these deformation mechanisms have been successfully reproduced in high-pressure static and dynamic experiments (Kirby and Christie 1977; Leroux et al. 1994). Among these, shock mechanical twins in pyroxene are considered diagnostic features of impact processes (Leroux et al. 2004, 2016; Daly et al. 2019). Nevertheless, the dislocation [001](100) glide system in pyroxene is not a diagnostic shock indicator due to its potential occurrence in mantle pyroxenite xenoliths (Henry et al. 2017). Furthermore, exsolution features are commonly observed in pyroxene from endogenic igneous or thermal metamorphic rocks (Ross et al. 1970; Bence and Papike 1972; Putnis 1992; Liu et al. 2007; Zhao et al. 2017), whereas only a few instances of pyroxene exsolution have been linked to shear stress at high temperature during shock events (Saxena et al. 1974; Mori and Takeda 1981; Takeda et al. 1982). As a result, distinguishing between shock and endogenic signatures in pyroxene remains challenging, particularly in materials that have experienced low-to-moderate degrees of shock.

To date, shock-induced deformations (e.g., plastic deformations, mechanical twinning, etc.) in pyroxene have rarely been investigated in lunar samples, and these features remain poorly characterized at high resolution (von Engelhardt et al. 1970; Schaal and Hörz 1977; Papike et al. 1998; Stöffler et al. 2018). The Chang'E-5 (CE-5) mission returned lunar samples from the northeastern Oceanus Procellarum, consisting of regolith assembled from local basaltic materials and shock-modified products. These samples provide a unique opportunity to study lunar magmatism and impact processes (Che et al. 2021; Qian et al. 2021b; Tian et al. 2021; Long et al. 2022; Luo et al. 2023; Wang et al. 2024; Wu et al. 2024). Studies at the CE-5 landing site have demonstrated that localized impact events, including small-scale collisions and micrometeorite bombardment, significantly alter the texture and geochemical properties of lunar regolith (Cao et al. 2022; Wu et al. 2023). Furthermore, these impact processes may induce measurable variations in pyroxene composition and structure when analyzed independently of crystallization conditions (e.g., magma composition, pressure, temperature, and oxygen fugacity). However, a critical uncertainty persists whether these observed variations in CE-5 pyroxene primarily reflect magmatic evolution processes or have been partially overprinted by post-crystallization impact modification. This ambiguity may introduce significant interpretative challenges when reconstructing magmatic histories based on pyroxene geochemical signatures, necessitating a more cautious approach when correlating mineralogical characteristics with magma evolution pathways.

In this study, we identify shock effects in a single pyroxene grain, including systematic deformation features, pigeonite exsolution, together with mechanical twins of ilmenite and impact melt veins within a shocked basaltic clast from the CE-5 lunar sample. Our study provides direct evidence of structural and compositional modifications in pyroxene under low-to-moderate shock conditions, highlighting the need to recognize shock microstructures before using pyroxene to infer magmatic processes.

Materials and Methods

The CE-5 mission's lunar regolith samples primarily originate from a uniform mafic source rock, with minor contributions from exotic materials. These samples exhibit widespread shock features, ranging from moderate to severe (Pang et al. 2022; Wu et al. 2023). The sample analyzed in this study is a ~300 μm basaltic clast that was manually selected from the drilled samples at a depth of ~10 cm in the lunar regolith by CE-5 lunar mission (sample CE5Z0906YJ, 200 mg). This clast was mounted in a thick section using epoxy resin, followed by coarse polishing with sandpaper of mesh sizes: 5000, 10 000, 15 000, and 20 000, and fine polishing using diamond powder with the grit sizes of 1, 0.3, 0.1, and 0.05 μm.

Polished sections were examined using a FEI Quanta 450 field emission scanning electron microscope (FE-SEM) equipped with an Oxford Instruments energy-dispersive spectrometer (EDS), and an Oxford Instruments HKL Nordlys II electron backscatter diffraction (EBSD) detector at the State Key Laboratory of Geological Processes and Mineral Resources, China University of Geosciences, Wuhan. Samples for EBSD analysis were uncoated for better pattern quality in a low-vacuum mode with the following working conditions: accelerating voltage of 20 kV, working distance of ~25 mm, sample tilt of 70°, and low-vacuum pressure of 20–30 Pa. Crystal structure files (match unit) for augite (augite, space group: *C*2/*c*, Salviulo et al. 1997), plagioclase (bytownite, space group: $P\bar{1}$, Fleet et al. 1966) and ilmenite (ilmenite, space group: $R\bar{3}$, Harrison et al. 2000) from the HKL database were utilized. EDS mapping of the basaltic clast (300 μm × 260 μm) was conducted simultaneously with EBSD mapping, using a step size of 0.5 μm. Additional backscattered electron (BSE) images were obtained at the Wuhan Sample Solution Analytical Technology Co., Ltd., Wuhan, China, using an analytical scanning electron microscope (JSM-IT100) connected to a GATAN MINICL system.

The quantitative analysis of major elements in minerals was performed in situ using an electron probe microanalyzer (EPMA, JXA-8230, JEOL) at Wuhan Sample Solution Analytical Technology Co., Ltd., Wuhan, and an electron probe microanalyzer (JXA-8230, JEOL) at the State Key Laboratory of Geological Processes and Mineral Resources, China University of Geosciences, Wuhan. The analytical conditions included an accelerating voltage of 15 kV and a beam current of 20 nA. The peak counting time for Ca, Ti, Si, Al, Ni, Fe, Mn, Cr, Na, Mg, K, and P is 10 s, with a background counting time of 5 s. Spot and line analyses were performed with a 1 μm beam diameter. Data were corrected using the ZAF correction method provided by JEOL, and standard reference materials were used as follows: Ca [$(Mg,Cr)CaSi_2O_6$], Ti [TiO_2], Si [SiO_2], Al [$Mg_3Al_2Si_3O_{12}$], Ni [Ni], Fe [Fe_2O_3], Mn [$MnSiO_3$], Cr [Cr], Na [$NaAlSi_3O_8$], Mg [$(Mg,Fe)_2SiO_4$], K [$KAlSi_3O_8$] and P [$Ca_5(PO_4)_3F$]. The liquidus temperature of the impact melt vein was determined using Rhyolite-MELTS (version 1.0.2), with oxygen fugacity calculated from bulk composition. Equilibrium conditions at 1 bar pressure were applied.

Raman spectra data were acquired using a WITec α300 confocal Raman imaging system at the State Key Laboratory of Biogeology and Environmental Geology, China University of Geosciences, Wuhan. Both single-point Raman spectroscopy and Raman spectral imaging were employed, with dwell times of 5–10 s and 0.4–0.6 s/pixel. The spectral resolution reached 0.1 relative wavenumbers. A 532 nm laser was used and focused under a 20× objective for large-area scans. Raman spectra were collected using a 50 μm diameter optic fiber, with a confocal depth of at least 1 μm below the polished surface. All Raman spectra were corrected for cosmic ray interference using the cosmic way reduction function in WITec Project Four Plus software.

Four thin foil specimens (6–20 μm × 6 μm × 100 nm) with 1–3 windows were prepared by focused ion beam (FIB) milling using a dual-beam Helios 5 CX FIB/FE-SEM at the Institute of Geochemistry, Chinese Academy of Sciences. Transmission Kikuchi diffraction (TKD) within the Helios 5 CX instrument was utilized for the identification of phases and their orientations at high-spatial resolution at Yanshan University. The same four foils were analyzed using a spherical-aberration-corrected scanning transmission electron microscope (STEM, Themis Z, Thermo Fisher, U.S.A.), equipped with a monochromator, operating at an accelerating voltage of 300 kV at Yanshan University. Bright-field (BF), annular dark-field (ADF), and high-angle annular dark-field (HAADF) images were obtained by combining 20 frames from the acquired series with drift correction (DCFI in Velox software, Thermo Fisher). The HAADF collecting angle was set at 65–200 mrad to eliminate effects of coherent scattering. Energy-dispersive spectroscopy (EDS) maps were obtained by a built-in X-ray energy-dispersive spectrometer (SuperX) in the Themis Z TEM instrument.

RESULTS

Petrography and Chemistry of the Lunar Basaltic Clast

The studied basaltic clast (~300 × 260 μm^2 in area) from CE-5 lunar soil is predominantly composed of pyroxene (87 vol%), with minor phases including plagioclase (9 vol%), ilmenite (4 vol%), troilite (<1 vol%), and silica glass (<1 vol%, Fig. 1 and Online Materials[1] Fig. S1). The clast is strongly fractured, with some regions even exhibiting amorphization (Figs. 1a–1b). In BSE and EDS mapping images, a large pyroxene grain (~250 μm in size) exhibits three distinct domains characterized by contrast heterogeneities, including deformed host domains, partially melted domains, and exsolution domains (Figs. 1a–1d). The deformed host domains have relatively homogeneous dark gray BSE contrast and are located in the interior of the pyroxene grain (Fig. 1a). In contrast, partially melted domains, closely associated with fractures in the pyroxene interior and along the pyroxene rim, display a light gray BSE contrast (Fig. 1a). These partially melted domains are filled with an amorphous matrix that is pyroxene-like in composition, along

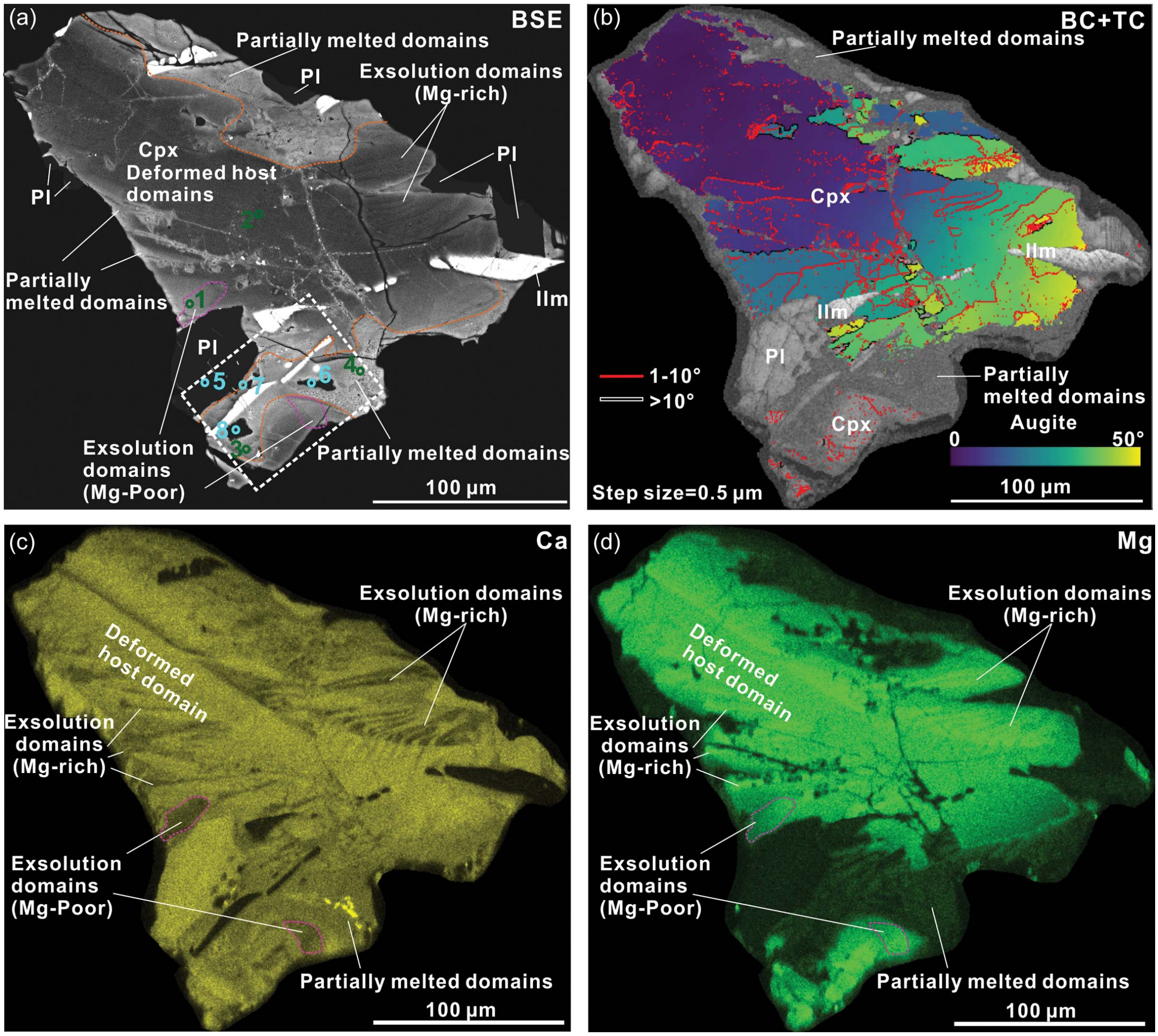

FIGURE 1. Microstructures and compositions of a shocked basaltic clast from CE-5 lunar regolith. (**a**) Backscattered electron (BSE) image showing clinopyroxene (Cpx), plagioclase (Pl), ilmenite (Ilm) with deformation features, circles from 1–8 indicate spot sites for Raman analysis; orange dashed lines are the boundaries for partially melted domains and host pyroxene, while purple dashed regions are exsolution domains (Mg-poor); (**b**) Band contrast (BC) and texture component (TC) maps for this basaltic clast, low-angle boundaries (1–10°) and high-angle boundaries (>10°) are overlaid on TC map; (**c**–**d**) X-ray intensity maps for Ca and Mg acquired via energy-dispersive spectrometry (EDS). Additional EDS maps are shown in Online Materials[1] Figures S2–S3. (Color online.)

with microscale to nanoscale silica-like glasses, ilmenite crystallites and troilite globules (Fig. 2). Some parts of the partially melted domains have recrystallized into pyroxene crystallites, which are classified as recrystallized regions (Figs. 2a and 2c). Exsolution domains exhibit an intermediate BSE contrast between deformed host and partially melted domains (Fig. 1a); these exsolution domains are embedded in irregular forms within the pyroxene interior and rim (Figs. 1a–1d). These three domains of pyroxene, specifically, deformed host domains, partially melt domains, and exsolution domains, reveal distinct differences in their Mg# values (Mg# = $Mg^{2+}/(Mg^{2+} + Fe^{2+}) \times 100$, Fig. 3, Table 1, and Online Materials[1] Table S1). The host deformed domains exhibit gradual variations of Mg# values, ranging from 19 to 55, while the partially melted domains show significantly lower Mg# values, ranging from 1 to 19. In contrast, exsolution domains display an intermediate but bimodal distribution of Mg# values with two distinct ranges: 22–30 and 44–53 (Table 1 and Online Materials[1] Table S1).

Deformed Host Domains

The deformed host domains exhibit strong Raman peaks of pyroxene at 1004, 665, and 320 cm^{-1}, along with additional Raman peaks at ~822 and 930 cm^{-1} (Fig. 4). The deformed domains of pyroxene retain whole-grain-scale plastic deformations with disorientations larger than 50° (Figs. 1b and 5a–5b). The glide system of dislocation [001](100) in deformed host domains is identified in pole figures (Figs. 5–6). Deformed host domains exhibit compositions of augite, $(Ca_{0.43–0.74}Mg_{0.22–0.73}Fe_{0.51–1.08})(Al_{0–0.05}Cr_{0–0.03}Mn_{0.01–0.02}Ti_{0.04–0.17})[(Si_{1.71–1.93}Al_{0.07–0.29})_2O_6]$, showing magmatic zonation of MgO-rich cores and FeO-rich rims (Fig. 1).

Exsolution Domains (Mg-rich and Mg-poor Pigeonite)

Exsolution domains have been identified based on the depletion of Ca, Al and Ti but enrichments in Mg, Fe, Si and O compared to the deformed host domains in EDS maps (Figs. 1c–1d and Online Materials[1] Fig. S1). These exsolution domains are further sub-classified into two types: (1) Mg-rich exsolution domains and (2) Mg-poor exsolution domains. The Mg-rich exsolution domains, $(Ca_{0.26–0.42}Mg_{0.72–0.84}Fe_{0.71–0.92})(Al_{0–0.02}Cr_{0–0.02}Mn_{0.01–0.02}Ti_{0.03–0.08})[(Si_{1.82–1.94}Al_{0.05–0.18})_2O_6]$, are located close to the interior of the host pyroxene, and the fractures at the rim of host pyroxene (Figs. 1a–1d). These Mg-rich exsolution domains appear in lamellar and wedge-like shapes and are closely associated with low-angle boundaries (1–10°, Figs. 6a–6f). They show enrichments in SiO_2 (~ × 1.1),

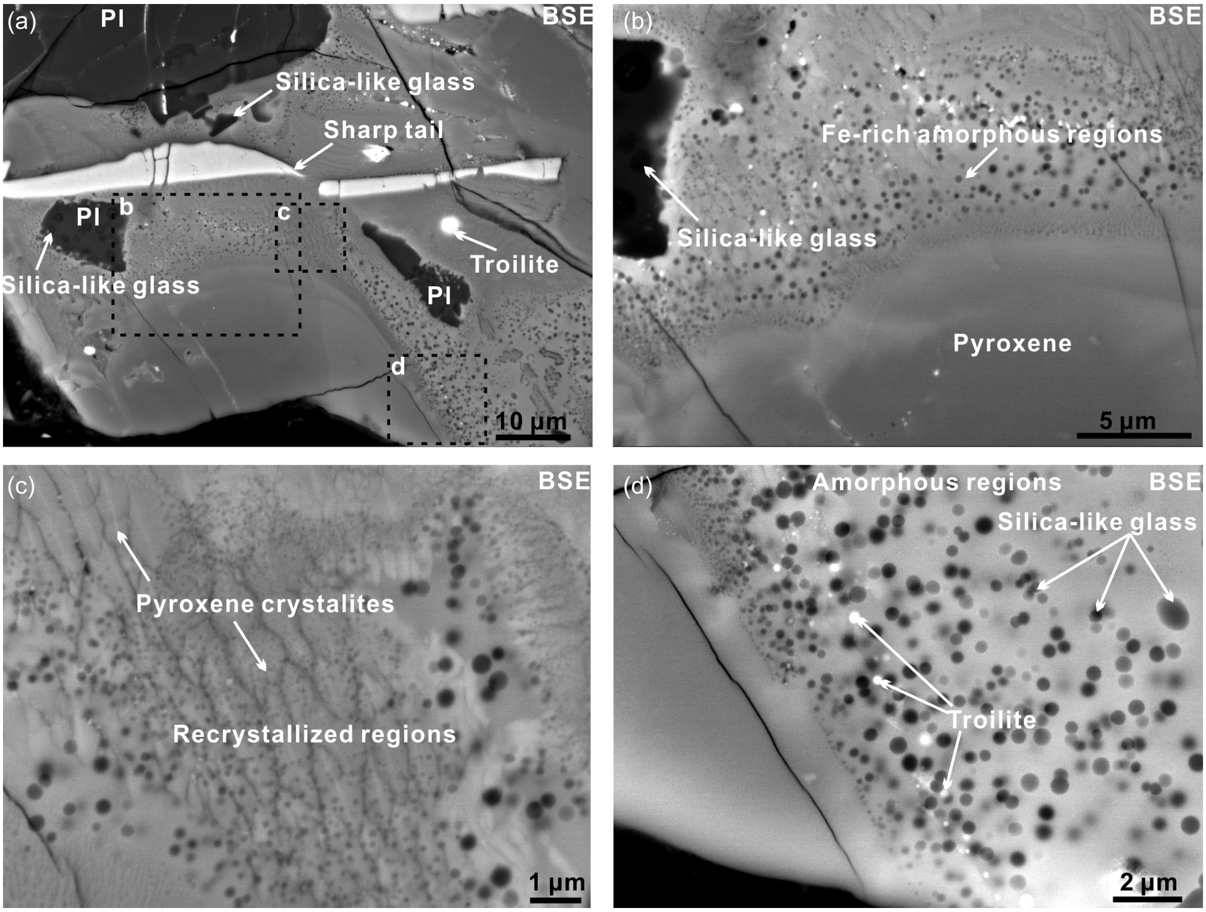

FIGURE 2. High-magnification BSE images of local partially melted domains in pyroxene. (**a**) Close-up view of the dashed box in Figure 1a; (**b–d**) partially melted domains containing melted pyroxene, plagioclase fragments, pyroxene crystallites, silica-like glasses, and troilite globules.

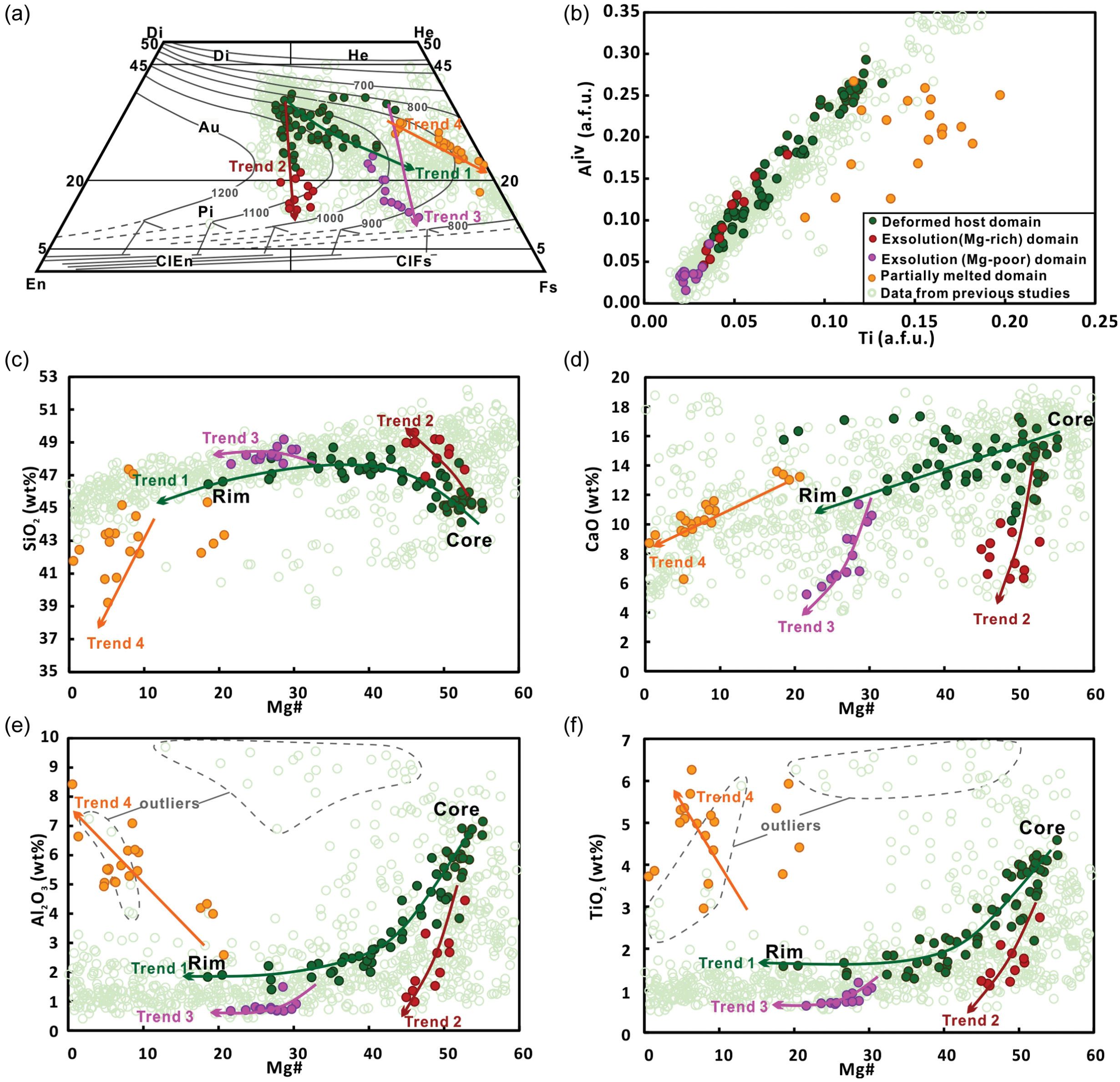

FIGURE 3. Composition variations of the shocked pyroxene. (**a**) Quadrilateral diagram illustrating different domains within the shocked pyroxene, the solvus isotherms of the two-phase field are from Lindsley and Andersen (1983); (**b**) ^{iv}Al–Ti diagram showing the atoms per formula unit (apfu) in pyroxene, pyroxene data from CE-5 lunar basalt show the trend approaching to ^{iv}Al/Ti = 2; (**c–f**) major element variations plotted against Mg#, green empty circles represent pyroxene data from CE-5 lunar samples (Wu et al. 2023 and references therein, Online Materials[1] Fig. S6). Trend 1 (green) represent the magmatic evolution, trend 2 (red, Mg-rich domain) and trend 3 (purple, Mg-poor domain) are exsolution processes, and trend 4 (orange) is the mixing trend by shock melting. Some outliers of previous pyroxene data are outlined by gray dashed lines. (Color online.)

FeO (~ × 1.3), and MgO (~ × 1.3) but depletions in Al_2O_3 (× 0.6–0.8), CaO (× 0.6–0.7), and TiO_2 (× 0.2–0.5) compared to adjacent deformed host domains (Figs. 1–3; Online Materials[1] Figs. S2–S4 and Table S1). The enrichment or depletion magnitude is calculated as the ratio of concentrations in the regions of interest to those in the deformed host domain ($C_{\text{Regions of interest}}/C_{\text{Deformed host domain}}$).

The Mg-poor exsolution domains, which occur in irregular shapes (patchy-like) at the rim of the host pyroxene and are also enclosed by the low-angle boundaries (1–10°), display lighter BSE contrast compared to the Mg-rich exsolution domains (Figs. 1a–1d). In these Mg-poor exsolution domains, $(Ca_{0.23–0.49}Mg_{0.37–0.46}Fe_{1.04–1.35})(Al_{0.02–0.07}Mn_{0.01–0.02}Ti_{0.02–0.04})[(Si_{1.93–1.98}Al_{0.02–0.07})_2O_6]$, the FeO content increases by 1.5–2 times while the Al_2O_3 (× 0.1–0.6), CaO (× 0.5), and TiO_2 (× 0.2–0.6) contents decrease from interior to rim compared to the deformed host domains (Figs. 1 and 3, Table 1, and Online Materials[1] Table S1). Some parts of the Mg-poor exsolution domains

TABLE 1. Representative EMPA data for different domains within shocked pyroxene

Domains	Deformed host domain	Exsolution domain (Mg-rich)	Exsolution domain (Mg-poor)	Partially melted domain
Sample	cpx-01r	cpx-1b	cpx-3r	am-02
SiO_2	45.36	46.64	48.78	41.88
TiO_2	3.78	2.71	0.75	5.80
Al_2O_3	5.77	4.39	0.67	3.91
Cr_2O_3	0.59	0.54	0.07	0.11
FeO	18.12	21.61	33.97	28.89
MnO	0.30	0.35	0.52	0.32
MgO	11.62	13.55	7.65	3.86
CaO	13.08	8.69	6.76	12.75
Na_2O	0.08	0.04	0.03	0.14
K_2O	bdl	0.01	bdl	0.13
Total	98.69	98.53	99.19	97.79
Numbers of ions based on 6 oxygen atoms				
Si	1.77	1.82	1.98	1.75
Al	0.26	0.20	0.03	0.19
^{iv}Al	0.23	0.18	0.02	0.19
^{vi}Al	0.03	0.02	0.01	0.00
Ti	0.11	0.08	0.02	0.18
Cr	0.02	0.02	0.00	0.00
Fe^{2+}	0.59	0.71	1.16	1.01
Mn	0.01	0.01	0.02	0.01
Mg	0.67	0.79	0.46	0.24
Ca	0.55	0.36	0.29	0.57
Na	0.01	0.00	0.00	0.01
Total cations	3.99	3.99	3.98	3.97
Wo	30.16	19.57	15.38	31.34
En	37.25	42.45	24.24	13.22
Fs	32.60	37.99	60.38	55.44
Mg#	53.33	52.77	28.64	19.25

Notes: These domains include the deformed host, exsolution (Mg-rich), exsolution (Mg-poor), and partially melted domains. "bdl" represents below detection limit.

adjacent to the partially melted domains present two additional peaks at ~822 and 930 cm^{-1} (Figs. 1a, 4a–4d, and Online Materials[1] Fig. S5), whereas other parts of the Mg-poor exsolution domains show the normal Raman peaks of pyroxene (Fig. 4a and Online Materials[1] Fig. S5).

Partially Melted Domains

The partially melted domain includes amorphous regions and recrystallized regions. The amorphous regions exhibit the distinct characteristic of Fe, Al, Si, Ti, K, and S enrichments but Mg and Ca deletions relative to the deformed host pyroxene (Figs. 1c–1d and Online Materials[1] Figs. S2–S3). These amorphous regions cannot be indexed by EBSD (Figs. 1b and 5a–5b) and exhibit broad and weak Raman peaks at 946 and 757 cm^{-1} (Fig. 4c). Recrystallized regions are dominated by pyroxene crystallites that are characterized by Raman peaks at 986, 925, 819, 657, and 344 cm^{-1}, which differ from the modes of the amorphous regions showing the broad Raman peaks at 757 and 946 cm^{-1} (Figs. 4c–4d). These pyroxene crystallites ($Wo_{30.9}En_{13.0}Fs_{55.5}$) have a higher Mg# value (19) and TiO_2 content, but lower Al_2O_3 content relative to the surrounding amorphous regions (Figs. 1–2; Online Materials[1] Figs. S2–S3 and Table S1). Moreover, the amorphous regions show distinct compositions, characterized by depletions in CaO and MgO contents but enrichments in FeO, TiO_2, and S contents compared to the deformed host domains (Figs. 1 and 3 and Online Materials[1] Figs. S2–S3). Local regions within amorphous regions exhibit enrichment in Ca and P, or Si and K, or S and Fe, suggesting the presence of apatite and troilite phases, and silica-like glasses in amorphous regions (Figs. 1 and 2 and Online Materials[1] Figs. S2–S3).

Microstructures and Compositions of Other Phases

Plagioclase grains, ranging in size from 10 to 40 μm, are observed surrounding pyroxene (Fig. 1a). Some fragmented plagioclase pieces (~10 μm) are enclosed within partially melted domains of pyroxene, exhibiting jagged margins (Fig. 2a). The plagioclase grains display a relatively homogeneous composition of $An_{77.6–82.3}Ab_{13.3–16.6}Or_{1–9}$ (Online Materials[1] Table S1). Raman spectra of plagioclase typically exhibit peaks at 403, 508, and 680 cm^{-1}, although the presence of silica-like or melted plagioclase glasses within the plagioclase grains weakens or broadens the Raman peaks at 508 and 680 cm^{-1} (Figs. 4e–4h). The silica-like glasses, which exhibit the darkest BSE contrast and appear as globules or irregular shapes (ranging from <1 to 10 μm in size), are closely associated with or embedded within plagioclase grains, as well as within the partially melted domains (Figs. 1–2).

Ilmenite grains are fragmented into several pieces ranging from <1 to 40 μm in size (Figs. 1a, 2, and 5). Some ilmenite fragments with sharp trails and similar orientation, potentially representing parts of a primary ilmenite grain, exhibit local sinistral displacement over a distance of >25–160 μm (Figs. 1a and 2a and Online Materials[1] Fig. S1). Smaller ilmenite fragments (<1 μm) are randomly distributed along fractures within pyroxene, while larger fragments (~40 μm) contain shock twins spaced 5–10 μm apart (Figs. 1a and 5c–5g). Two sets of ilmenite twins, oriented along $\{10\bar{1}1\}$ and (0001), are observed within a large, fragmented ilmenite host (Figs. 5c–5d and 5f–5g). Troilite occurs as <5–10 μm globules within the partially melted domains (Figs. 2a–2d).

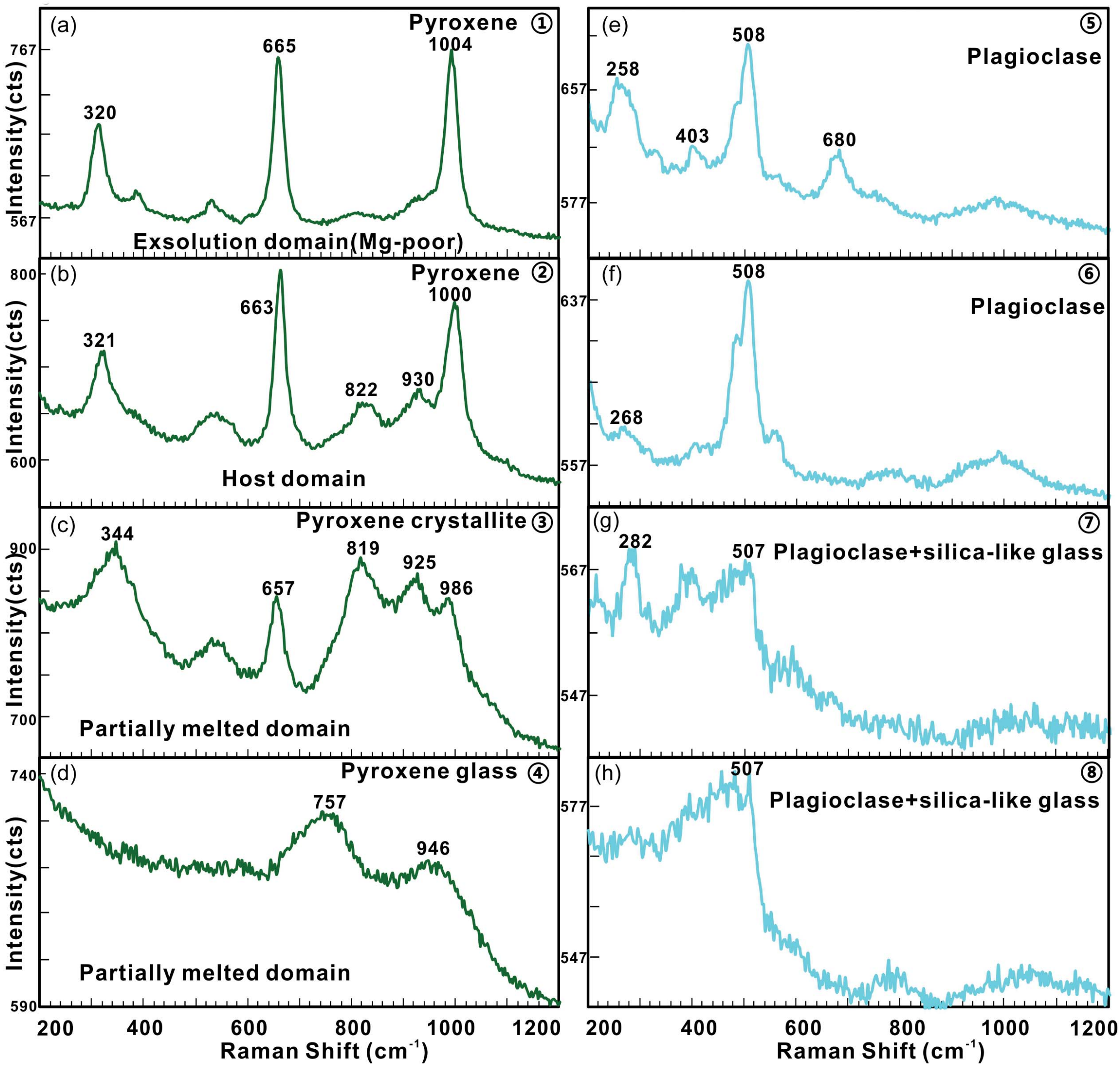

FIGURE 4. Raman spectra for shocked pyroxene and plagioclase, the number locations (1–8) correspond to the analysis sites shown in Figure 1a, with sites 1–4 representing pyroxene regions and sites 5–8 representing plagioclase regions. (Color online.)

Nanoscale Observations on the Partially Melted and Exsolution Domains in Pyroxene

Four foils cut by focused ion beam (FIB) were extracted from the partially melted and exsolution domains (foils 1–4, Figs. 5a and 7 and Online Materials[1] Fig. S1). Nanoscale phases are identifiable in HAADF and EDS maps, where silica-like glasses exhibit distinct high concentrations of Si and K; troilite is characterized by high concentrations of Fe and S; and ilmenite crystallites are characterized by significant concentration of Ti and Fe (Figs. 8 and 9a–9c). Foil 1 consists of silica-like glass, troilite, ilmenite, pyroxene, apatite, and amorphous matrix (with 2 windows, Fig. 7a). Foil 2 exhibits the boundary characteristics between the partially melted and deformed host domains of pyroxene (with 1 window, Fig. 7b). Foil 3 displays the contact relationship between ilmenite and partially melted domains (with 3 windows, Fig. 7c). Foil 4 displays the morphology of exsolved phases (pigeonite) within Mg-rich exsolution domains (with 3 windows, Fig. 7d). No pyroxene shock twins were observed in foils 1–4 (Figs. 7–9).

Liquid Immiscibility Within Partially Melted Domains

Silica-like glass and troilite can occur as globules (20–1500 nm in size) associated with the pyroxene, apatite, and ilmenite crystallites (2–5 μm in size), or they can be found randomly within the Fe-rich amorphous matrix (Figs. 7a–7c and 8). This immiscibility phenomenon can be attributed to the phase separation between silica-like glasses and Fe-rich silicate matrix, as well as the immiscible behavior between sulfides

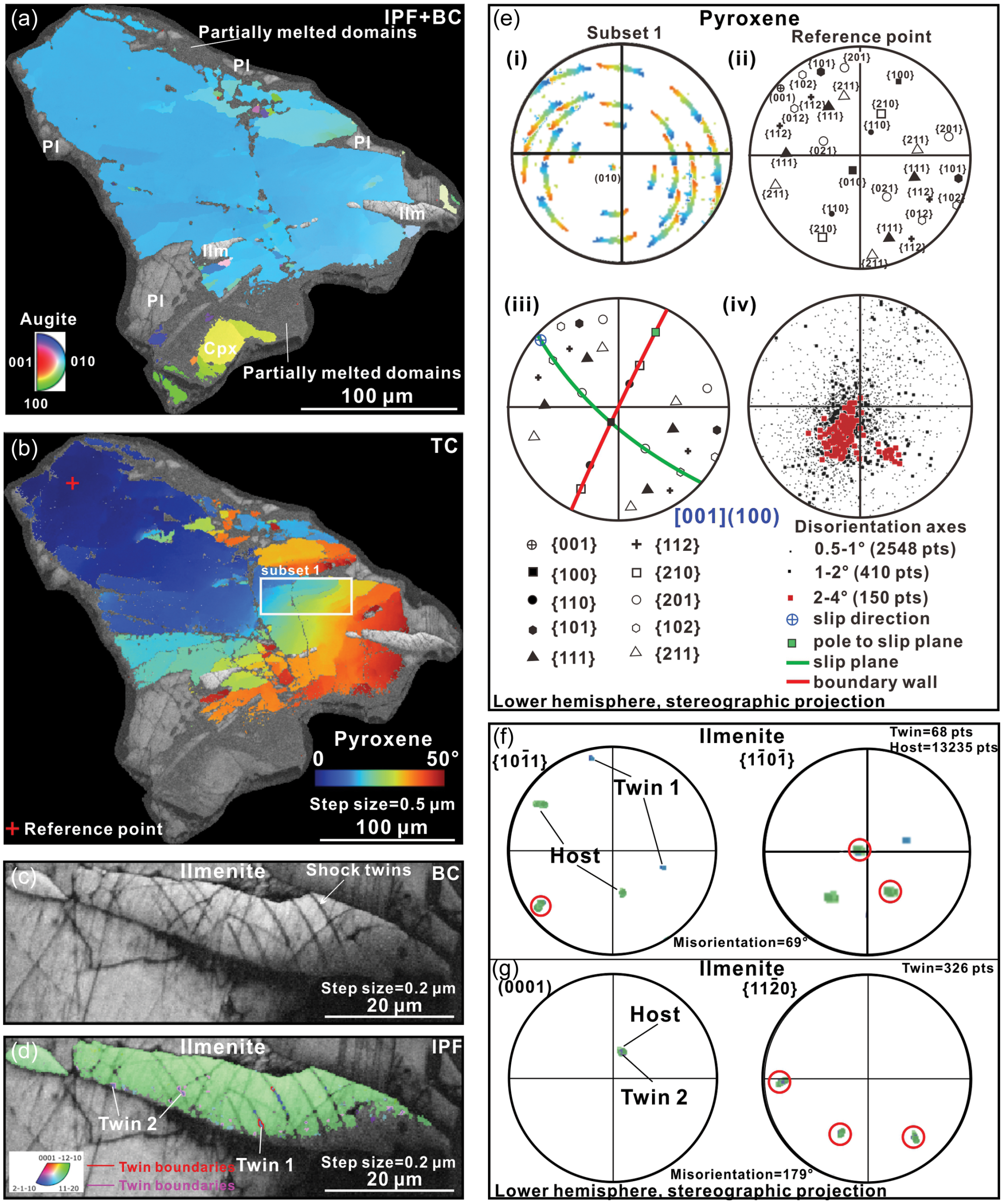

FIGURE 5. Microstructures in pyroxene and ilmenite mapped by electron backscattered diffraction (EBSD). (**a**) Inverse pole figure (IPF) map for the shocked basaltic clast; (**b**) texture component (TC) map for the shocked pyroxene, the red cross is the reference point, white rectangle is the region for subset 1; (**c**) BC map of ilmenite showing shock twins; (**d**) IPF map for ilmenite; (**e**) pole figures for the shocked pyroxene with the same color scheme as in **b**, i and ii are plotted by data from Subset 1 and reference point in **b**, the [001](100) glide system is evidenced by the rotation axis of {010} in the pole figure, the {010} rotation axis (iii) is consistent with the distribution of the disorientation axes (iv), plastic deformation in pyroxene is characterized by the methods from Reddy et al. (2007); (**f–g**) pole figures of ilmenite, using the same color scheme as in **d**, the red circles in **f** and **g** highlight the aligned planes between the twin and host of ilmenite. (Color online.)

and the silicate matrix in the liquid state. The nanoscale silica-like globules (~100 nm in size) intensively aggregate, approaching microscale silica-like glasses (~5 μm in size), which are located together with the plagioclase fragments at the bottom-right of the foil 1 (Fig. 7a). This suggests that the nanoscale silica-like globules are released from the microscale silica-like glass during the formation of impact melt veins, as observed in BSE images of microscale silica-like glasses that coexist with plagioclase fragments (Figs. 1–2).

In foil 3, some immiscible silica-like glasses adjacent to an unfused ilmenite slab within the partially melted domains are elongated into elliptical shapes (Fig. 7c). Similarly, the long

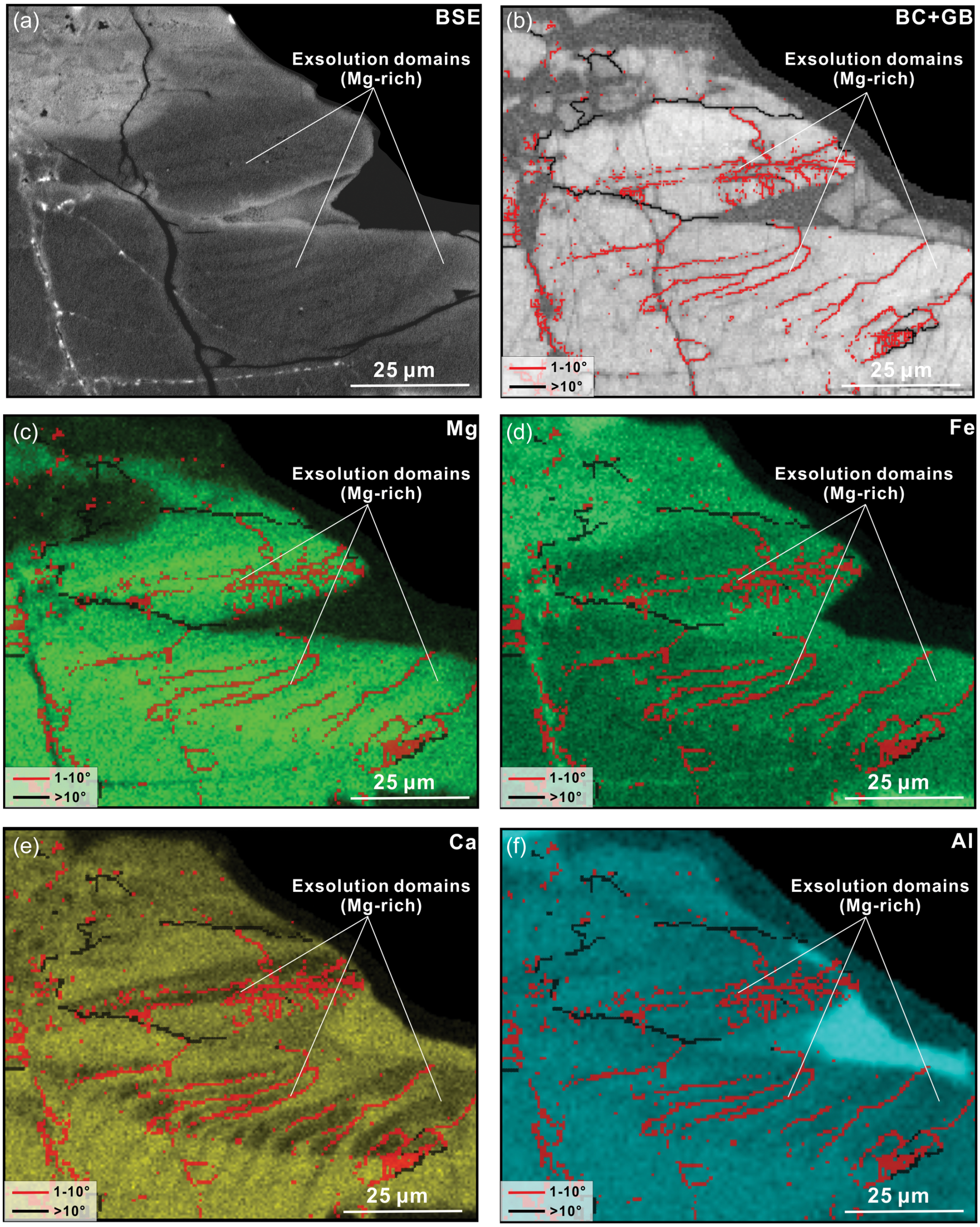

FIGURE 6. Elemental distribution and microstructural features within the exsolution domains of pyroxene. (**a**) Close-up BSE image of the exsolution domains; (**b**) close-up BC map overlaid with the low-angle (1–10°) and high-angle boundaries (>10°); (**c–f**), close-up EDS and grain boundary (GB) maps showing the distribution of Mg, Fe, Ca, and Al within the exsolution domains. (Color online.)

axes of the troilite and ilmenite crystallites, which are aligned parallel to the ilmenite slab, exhibit the same elongation direction (Fig. 7c). In particular, in localized regions, elongated silica-like glasses are observed in two distinct orientations, exhibiting linear or tadpole-like morphologies. Their dimensions vary in length (500–1600 nm), width (10–30 nm), and spacing (50–60 nm), respectively (Figs. 8b–8d).

Boundary Layers Between Partially Melted Domains and Host Pyroxene

Partially melted domains are located within the fractures of the host pyroxene or surrounding the rim of host pyroxene in foil 2 (Fig. 7b). The partially melted domains are predominantly composed of pyroxene dendrites (~150–500 nm in size), along with a few troilite and ilmenite crystallites (10–300 nm in size),

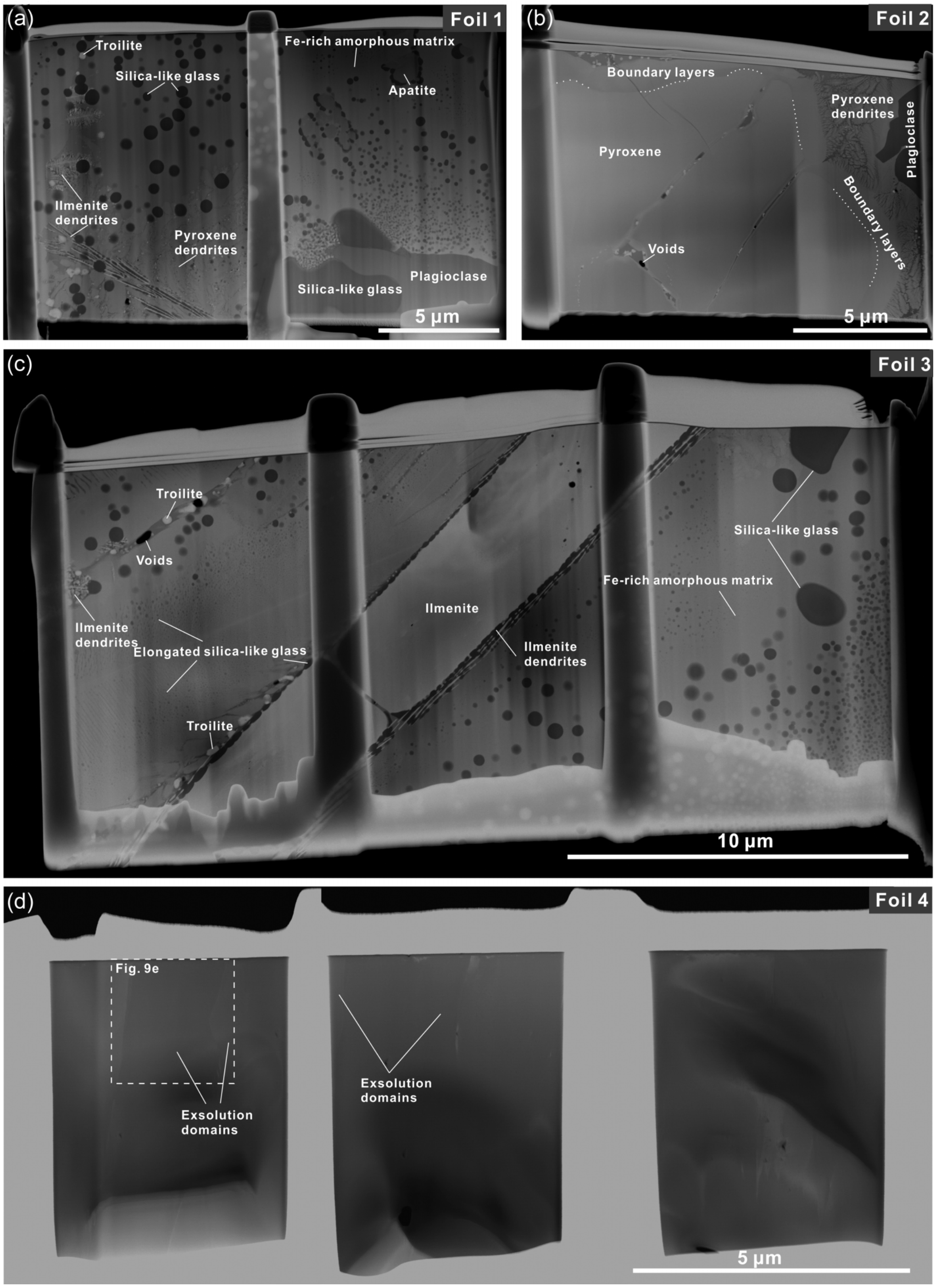

Figure 7. High-angle angular dark-field (HAADF) images for FIB-cut foils (1–4), with the cutting sites indicated in Online Materials[1] Figure S1. (**a**) Foil 1 reveals the nanoscale phases present in partially melted domains; (**b**) Foil 2 illustrates the boundary features between host pyroxene and partially melted domains; (**c**) Foil 3 displays an unmelted slab within the partially melted domains; (**d**) Foil 4 highlights the exsolution domain, the dashed box was the region examined by TKD mapping in Figure 9e.

suggesting that the partially melted domains in foil 2 were primarily formed due to the localized melting of pyroxene with minimal involvement of other phases (Fig. 7b). Similarly, the fractures within the host pyroxene contain minor ilmenite and troilite crystallites, along with amorphous materials and voids (Fig. 7b). The boundary layers (30–200 nm thick) between the host pyroxene and pyroxene dendrites exhibit homogeneous HAADF contrast similar to that of the pyroxene dendrites (Fig. 7b). In contrast, EDS maps reveal a gradual variation in CaO, MgO, and FeO concentrations along the transition from pyroxene dendrites to host

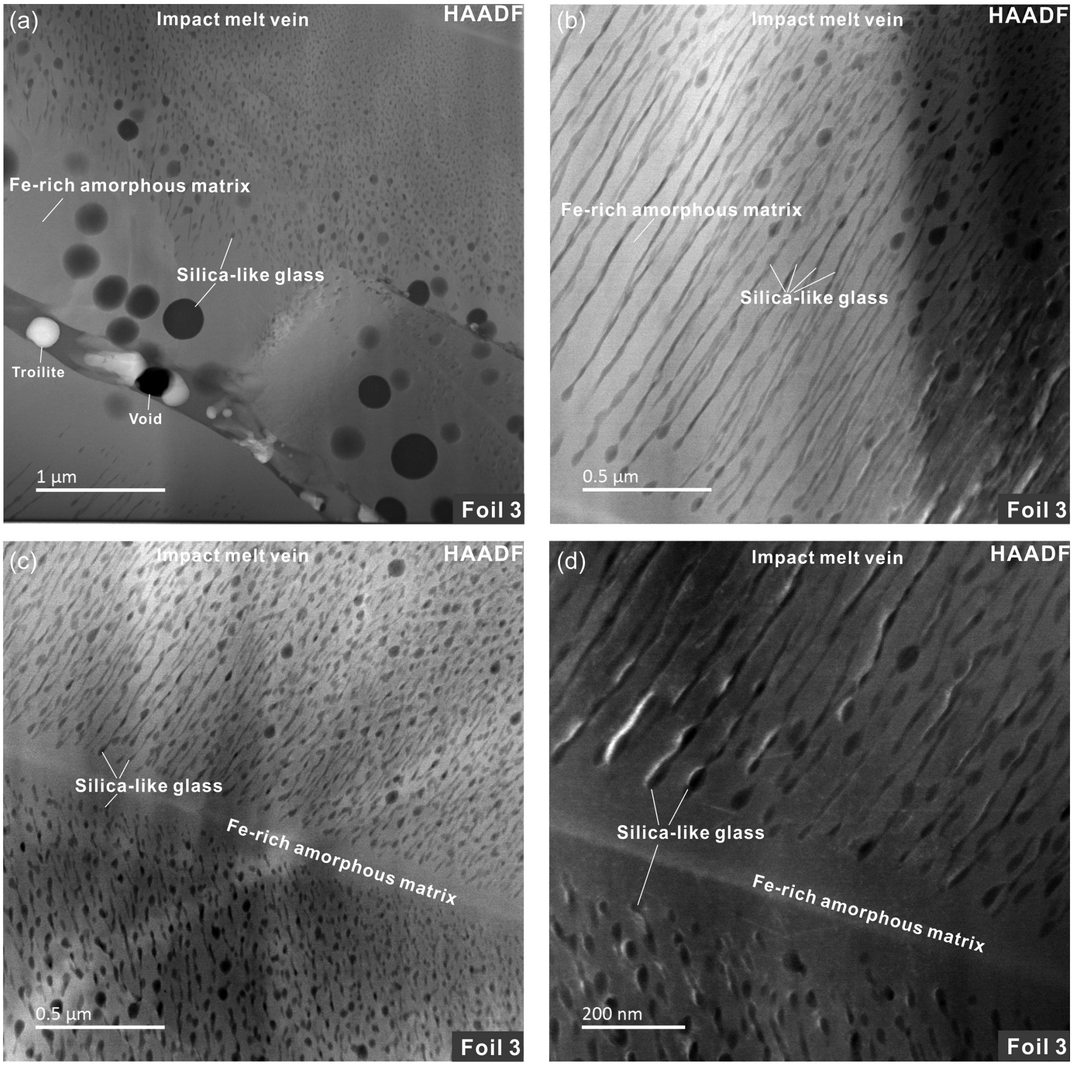

FIGURE 8. Various forms of silica-like glass in partially melted domains of pyroxene (foil 3). (**a**) Troilite and silica-like globules; (**b**–**d**) close-up images of elongated silica-like globules at the nanoscale.

domains. Boundary layer domains adjacent to pyroxene dendrites, enriched in CaO and FeO, corresponds to augite, while the layer closer to the host domain appear as pigeonite with MgO enrichment (Fig. 9d). These boundary layers exhibit compositional variations at the microscale similar to those observed via EDS in exsolution domains (Figs. 1c–1d and 9d and Online Materials[1] Fig. S7).

Nanoscale Morphology and Composition of Exsolution Domains

Exsolution domains in HAADF images display a relatively homogeneous phase of pyroxene in foil 4 (Fig. 7d). Some regions show different contrasts after excluding the thickness effects (where thicker regions of foil display brighter contrasts than thinner regions), reveal notable variations (Fig. 7d). Multiple irregular forms of pigeonite exsolution are characterized by a depletion of Ca and an enrichment of Fe and Mg, as clearly shown in EDS maps (Fig. 9e). Furthermore, the Ca distribution is closely associated with lattice defects within the pyroxene, as depicted in the BC map, while the distribution of other elements, such as Fe and Mg, is observed to be spatially distant from these lattice defects (Fig. 9e). The lattice defects, indicated by the BC map, correspond to low-angle boundaries, which trace the observed Ca enrichments (Fig. 9e). The Mg-rich exsolution domains observed in FIB foil 4 at the nanoscale are consistent with observations in both BSE and EBSD maps at the microscale, in terms of both morphology and composition.

DISCUSSION

Shock Localized Melting Induced By Shear Frictional Processes

The pyroxene grain is affected by pervasive intra-crystalline plastic deformations, including the dislocation [001](100) glide system and cumulative disorientations up to 50° (Figs. 1b, 5, and 6). In clinopyroxene, the dislocation [001](100) glide system

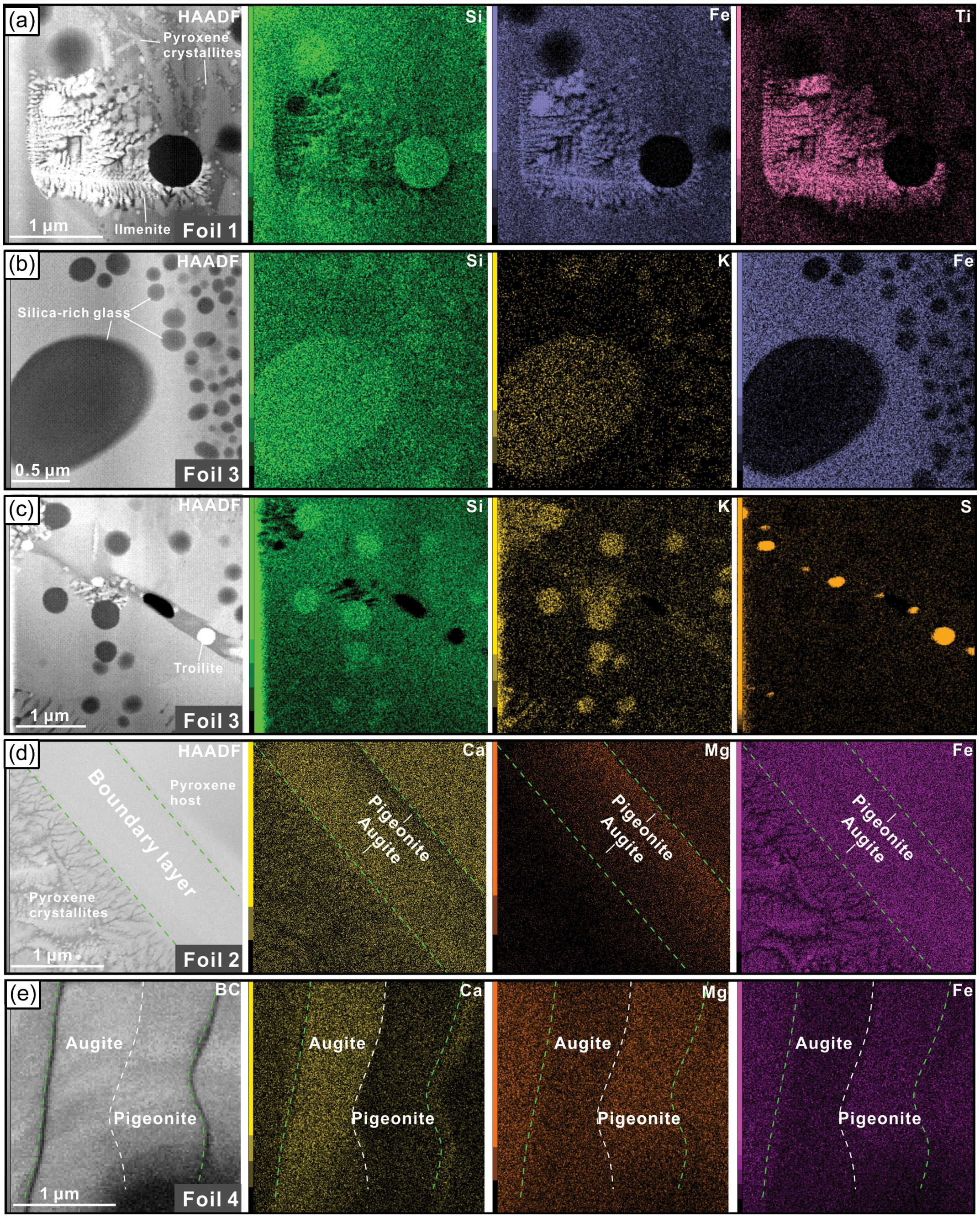

Figure 9. Nanoscale morphological and compositional features in partially melted and exsolution domains. (**a**–**c**) HAADF images and corresponding EDS maps for ilmenite crystallites, silica-like glasses, and troilite; (**d**) boundary features between the partially melted and host domains; (**e**–**f**) exsolution features illustrated by BC and EDS maps. (Color online.)

typically forms at high strain rates ($\Upsilon > 10^2$ s^{-1}) during impact events (Langenhorst et al. 1995), or at high temperatures (>1000 °C) in the upper Earth mantle (Henry et al. 2017). However, mechanical twins parallel to $\{10\bar{1}1\}$ and (0001) rather than tectonically deformed twins parallel to $\{10\bar{1}2\}$ in ilmenite, identified via pole figures and IPF maps (Figs. 6c–6d and 6f–6g), suggest a shock origin (Minkin and Chao 1971; Schaal and Hörz 1977; Stöffler et al. 1986; Dellefant et al. 2022). Based on experimental and lunar sample data, this constrains the shock pressure to 9–100 GPa (Minkin and Chao 1971; Schaal and Hörz 1977; Stöffler et al. 1986). Notably, similar ilmenite twins in the Archean gneisses from the Vredefort impact crater record pressures less than 20 GPa under the non-isostatic shock conditions (Dellefant et al. 2022). Further evidence for low-to-moderate peak pressures includes: (1) the absence of planar deformation features (PDFs) in pyroxene (Figs. 5 and 7), excluding pressures >30 GPa

(Fritz et al. 2005; Filiberto et al. 2018; Stöffler et al. 2018), and (2) plagioclase fragments lacking maskelynization, which requires pressures >17 GPa (Hu et al. 2023). Collectively, these features limit the bulk peak shock pressure in this clast to 9–17 GPa.

The low-to-moderate shock pressure indicated by the deformations in host pyroxene and ilmenite is insufficient to induce the incipient melting of phases in this basaltic clast (Fritz et al. 2017; Koeberl and Henkel 2005). Nevertheless, the non-isostatic shock conditions, revealed by distinct displacements and deformation morphologies (e.g., sharp tails, Figs. 1a and 2a) of ilmenite, support the possibility that localized frictional melting processes could drive the formation of partially melted domains within or surrounding the pyroxene host. Frictional processes can generate localized high temperatures, leading to the formation of impact melt veins under relatively low shock pressures (Koeberl and Henkel 2005; Spray 2010; Walton et al. 2016; Fritz et al. 2017). Although no high-temperature phases indicate the peak temperature within the impact melt veins, MELTS software calculations, using the major-element composition of impact melt veins, suggest solidus temperatures for the partially melted domains range from 1084 to 1239 °C. These temperatures represent the lower limit for the formation of impact melt veins. Furthermore, higher titanium concentration in partially melted domains compared to host deformed domains (Online Materials[1] Fig. S3a) suggests that the addition of melted ilmenite into partially melted domains, where local temperature can reach the melting point of ilmenite ($FeTiO_3$, ~1470 °C, Spray 2010). Consistently, shearing, evidenced by ilmenite fragments with sharp tails in deformed host domains of pyroxene, is associated with distinct displacement distances exceeding 25 μm (Figs. 1a–1b and 5a and Online Materials[1] Fig. S6). The shear process can be simulated using a two-plane frictional model (Cardwell et al. 1978) based on the observed average width of the melt vein (w = ~20 μm), displacement distance (d = 25–160 μm), and peak temperature (>1239–1470 °C). Thus, the estimated time (τ) required for frictional melting to reach peak temperature is 0.06 to 2.4 ms (Fig. 10a, Online Materials[1] S8). Accordingly, the strain rate ($\Upsilon = d/\tau w$, $>10^4\ s^{-1}$) calculated for the melt vein aligns with the formation conditions ($\Upsilon = 10^{-2}$ $-10^8\ s^{-1}$) observed in shock melt veins and pseudotachylyte in previous studies (Langenhorst and Poirier 2000; Spray 2010), confirming that frictional processes effectively facilitate the formation of impact melt veins in this shocked pyroxene.

The silica-like globules within the partially melted domains (Figs. 2a, 7a–7c, and 8a) are compositionally similar to the Si-rich phases in interstitial mesostasis pockets from CE-5 and other lunar basalts (He et al. 2022; Pernet-Fisher et al. 2014; Wu et al. 2023). Mesostasis pockets consist of a mixture of Si-rich glasses, fayalite, apatite, K-feldspar, and troilite, which form after the crystallization of pyroxene and plagioclase during the late stage of lunar basalt formation (Pernet-Fisher et al. 2014; He et al. 2022; Wu et al. 2023). Nevertheless, the silica-like glasses observed in the partially melted domains in this study differ from primary mesostasis pockets in two aspects: (1) the partially melted domains do not resemble the primary textures and compositions of interstitial mesostasis pockets from CE-5 and other lunar basalts (Pernet-Fisher et al. 2014; He et al. 2022; Wu et al. 2023); (2) elongated silica-like glasses are locally presented at the nanoscale (Figs. 8a–8d), which is inconsistent with the typical forms of Si-rich glasses in interstitial mesostasis pockets (Jin et al. 2024), and experimental studies (Veksler et al. 2007, 2008). Therefore, the mesostasis materials with a relative lower melting temperature than other phases (pyroxene, plagioclase, and ilmenite) were initially reworked and incorporated into the partially melted domains during the formation of impact melt veins.

The presence of the elongated silica-like glasses in impact melt veins (Figs. 8a–8d) suggests a dynamic, non-isostatic formation and solidification setting, unlike the static solidification of interstitial mesostasis pockets in lunar basalts. This phenomenon could be explained by frictional melting during shock loading could generate rapid melt motion, inducing relative movements between silica-like glasses and the Fe-rich immiscible matrix due to differences in density and viscosity (Veksler et al. 2008). Furthermore, this interpretation requires that the solidification of an impact melt vein occurred nearly simultaneously with the cessation of frictional melting, which is essential for retaining the deformations of silica-like glasses that formed in a liquid state. Otherwise, the silica-like glasses would likely have been dispersed as much smaller globules in a relatively static state due to the immiscibility, as seen in the most common occurrences of silica-like globules in Figures 7a–7c. The solidification time is modeled by the cooling of a thin slab (w = ~20 μm) by releasing the latent heat of melt and solidifying from each side of the impact melt vein to its center (Langenhorst and Poirier 2000). The modeled solidification time of ~120–160 μs (Fig. 10b and Online Materials[1] S9) from the peak temperature (>1239 °C) suggests a very quick solidification process to retain the shear deformations of silica-like glasses. Therefore, frictional melting likely drives the formation of impact melt veins in a dynamic situation during shock loading, resulting in the deformations of silica-like glasses in impact melt veins that were solidified quickly.

Structure Variations In Locally Shock-Melted and Recrystallized Pyroxene

Four systematic types of Raman spectra have been recognized from the following domains in this single pyroxene: host deformed domains, exsolution domains (Mg-rich and Mg-poor), partially melted domains (Figs. 4a–4d), indicating the successive structural adjustments in the pyroxene lattice in response to impact deformation. Only some parts of the Mg-poor exsolution domains of pyroxene reveal the normal Raman modes for pyroxene (Fig. 4a), compared with previous studies (Huang et al. 2000; Wang et al. 2001). Two additional peaks at 930 and ~822 cm^{-1} were found in the deformed host domains and other exsolution domains (Fig. 4b and Online Materials[1] Fig. S5), in addition to the normal Raman peaks of pyroxene. The 930 cm^{-1} Raman peak has been attributed to a weak stretching mode of non-bridging Si–O bonds in pyroxene (Huang et al. 2000) or to a critical Raman peak in majorite (Zhang et al. 2006). However, STEM analysis confirms that no majorite is present in this impact melt vein (Figs. 2 and 7). Hence, the 930 cm^{-1} peak is most likely due to the stretching mode of non-bridging Si–O

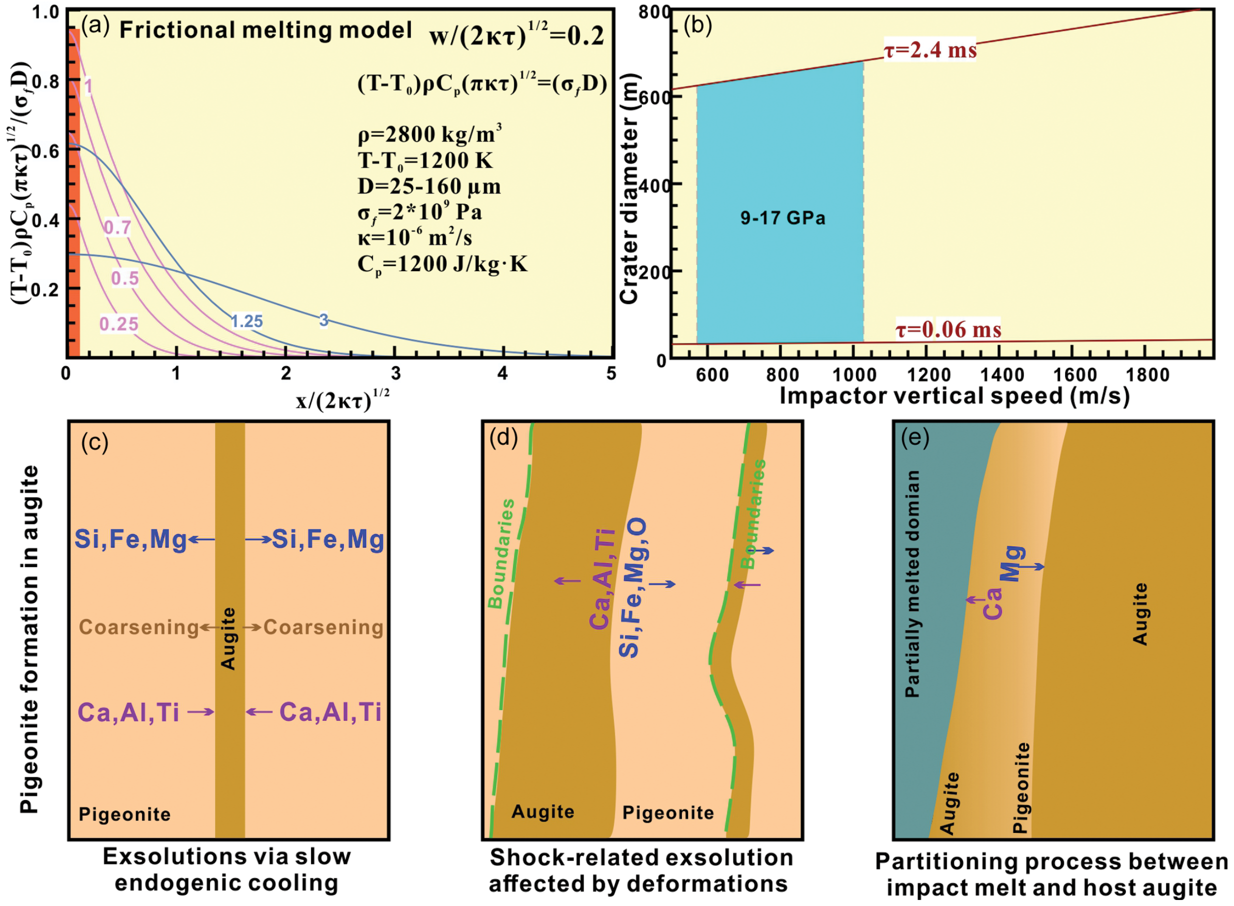

FIGURE 10. Models for shock shear heating and cooling processes, pyroxene exsolution, and estimation of impact crater size. (**a**) Frictional melting model with a finite width of the melt vein, based on Cardwell et al. (1978). Given the rapid shear and cooling indicated in Figures 1, 2, and 8, we assume the heat conduction distance is much larger than the width of the impact melt vein during the shock duration, i.e., $w/(2\kappa\tau)^{1/2} << 1$, where w is the impact melt vein width and τ is the shock loading (shear) duration. The shock loading duration is modeled to be 0.06–2.4 ms (Online Materials[1] S8); the pink and blue lines represent the heating and cooling with the time ($t' = 0.25, 0.5, 0.75, 1, 1.25, 3$); the impact melt vein reaches to the peak temperature when $t' = 1$. (**b**) Diameters of the impact craters on the Moon as a function of the vertical impact speed (Beck et al. 2005). The crater size is estimated to be larger than 30–600 m. (**c**–**e**) Three pigeonite formation models via slow endogenic cooling, shock-related exsolution affected by deformations, and partitioning processes between impact melt and host augite. (Color online.)

bonds in pyroxene (Huang et al. 2000; Wang et al. 2001). Similarly, the 822 cm^{-1} Raman peak, which has been associated with a typical Raman peak of olivine (fayalite), is ruled out based on observations in BSE and HAADF images (Figs. 2 and 7). Instead, numerical calculations suggest that the stretching mode of non-bridging Al–O bonds, with a Raman peak at ~818 cm^{-1}, corresponds to Ca-Tschermak pyroxene ($CaAl_2SiO_6$) (Dowty 1987). Therefore, the possibility of Si–O bonds replaced by Al–O bonds in this shocked pyroxene is evaluated below.

The amorphous regions within partially melted domains are characterized by two broad peaks at ~757 and 946 cm^{-1} (Fig. 4d), which resemble those observed in pyroxene glasses (Cao et al. 2022; Feng et al. 2017; Imae and Ikeda 2010). Notably, the amorphous regions lack the strong Si–O–Si bridging bonds, which typically exhibit a stretching mode at ~651 cm^{-1} (Sharma et al. 1983). This absence indicates a complete disruption of the Si–O tetrahedral chain in amorphous regions. Broad peaks corresponding to non-bridging T–O bonds (T = Si or Al), ranging from 994 to 946 cm^{-1}, have been reported in amorphous glass with a pyroxene-like composition in previous studies (Sharma et al. 1983; Imae and Ikeda 2010; Feng et al. 2017; Cao et al. 2022). These findings support the interpretation that the stretching mode induced by the non-bridging Al–O bonds, replacing the non-bridging Si–O bonds in the tetrahedron of the pyroxene structure, contributes to variations in Raman peaks ranging from ~1000 to ~948 cm^{-1}, consistent with high Al content in the amorphous regions (Online Materials[1] Fig. S2f).

The recrystallized regions exhibit slightly distinct Raman peaks at 657, 819, 925, and 986 cm^{-1} due to the growth of pyroxene crystallites (Figs. 2c and 4c). The chain of Si–O tetrahedron incorporating some Al–O bonds is formed in pyroxene crystallites, which is indicated by the occurrence of bridging Si–O–Si bonds (657 cm^{-1}) and non-bridging Al–O bonds (986 cm^{-1}, Sharma et al. 1983). The pyroxene crystallites within recrystallized regions rapidly crystallized from the amorphous materials that have the lowest SiO_2 content, but the highest Al_2O_3 and TiO_2 contents, also show the typical Raman peak of ~822 cm^{-1} (Fig. 4c and Online Materials[1] Figs. S2f and S3a), similar to the observations in impact glasses from CE-5 regolith (Wu et al. 2023). The mechanism of Al-Si substitution in pyroxene crystallites within recrystallized regions is facilitated by fast crystallization, causing the increase of Al instead of Si at the tetrahedron site in clinopyroxene in rapid crystallization experiments (Mollo et al. 2010), associated with the occurrence of 818 cm^{-1} observed in Ca-Tschermak pyroxene (Dowty 1987). Therefore, Al-Si substitution by localized rapid melting and crystallization processes in pyroxene can result in the Raman peaks at 1000–946 and 822 cm^{-1}.

Exsolutions in Pyroxene by Endogenic Cooling or Shock-Induced Processes?

The exsolution of magmatic pyroxene into two phases (e.g., augite and pigeonite, augite and orthopyroxene) has been widely observed in samples from Earth's crust and mantle, lunar basalts, martian meteorites, HED meteorites, and other extraterrestrial materials (Ross et al. 1970; Takeda et al. 1982; Putnis 1992; Miyamoto et al. 2001; Leroux et al. 2016; Pittarello et al. 2019). Most exsolution phenomena are attributed to slow endogenic cooling processes, occurring within the shallow or deep crust of a planet as temperatures decrease from ~1100 to 800 °C, primarily driven by thermal effects (Takeda et al. 1975; Miyamoto and Takeda 1977; Takeda et al. 1982; Miyamoto et al. 2001). However, only a few exsolution processes are influenced by other factors, such as pressure variations and associated deformations induced by tectonic activity (Kirby and Etheridge 1981; Zhao et al. 2017) or impact events (Mori and Takeda 1981; Takeda et al. 1982). Exsolution domains (pigeonite) within host augite in this study have been revealed by typical element enrichments in MgO and FeO but depletions in CaO (Figs. 1c–1f, 2a–2c, and 6a). Therefore, a debate has arisen regarding the formation mechanism of the exsolution processes observed in shocked pyroxene in this study, specifically whether they are the result of endogenic cooling processes or shock-induced processes. Three aspects of evidence, including exsolution morphology, exsolution composition, and nanoscale observations, have been evaluated as follows.

Constraints From Exsolution Morphology of Pigeonite

During the slow endogenic cooling of magmatic systems, pyroxene minerals undergo a series of transformations influenced by temperature. Initially, high-temperature crystallization yields augite. As cooling progresses, this augite can exsolve to form lamellae of pigeonite and augite. If the cooling rate is sufficiently slow, pigeonite may further invert to orthopyroxene (Ross et al. 1970; Putnis 1992; Pittarello et al. 2019). The morphology and orientation of these exsolution lamellae are critical for interpreting the thermal history of the host rock. For instance, the thickness and spacing of pigeonite lamellae within an augite host, or vice versa, can be utilized to estimate cooling rates and the depths at which the rock was buried within the crust (Miyamoto and Takeda 1977; Grove 1982; Takeda et al. 1982; Miyamoto et al. 2001). Studies have demonstrated that slower cooling rates allow for the development of coarser lamellae, indicative of deeper crustal levels and prolonged thermal regimes (Miyamoto and Takeda 1977; Grove 1982; Takeda et al. 1982; Miyamoto et al. 2001). Therefore, lamellar exsolution in pyroxene is a common feature of slow endogenic cooling processes.

However, in this study, the exsolved pigeonite does not strictly exhibit a lamellar form both at the microscale and the nanoscale (Figs. 1a–1d, 6, and 9d–9e). A comparison of exsolution morphology between this study and previous studies is necessary. The pyroxene grains from shocked martian meteorites (NWA 856 and 7533) show the co-occurrence of shock twins, exsolution lamellae (pigeonite/augite), and dislocation [001](100) glide system (Leroux et al. 2004, 2016). In these studies, exsolution lamellae in pyroxene are related to the slow endogenic cooling processes, whereas mechanical twins and dislocation [001](100) glide system result from shock processes (Leroux et al. 2004, 2016). There are some similarities between the previous findings in martian pyroxene and observations in this study; for example, the presence of exsolution and glide system in shocked pyroxene. Nevertheless, exsolved pigeonite in this study is in irregular forms with different orientations, shapes, and thicknesses (Figs. 1c and 6). Furthermore, most of the exsolution domains are coincidentally associated with the distributions of low-angle boundaries (<1° and 1–10°, Fig. 6), which accumulated and developed as the glide system of [001](100) dislocation at the grain scale (Figs. 5–6). Similarly, nanoscale observations also suggest that the pigeonite phases, which do not conform to lamellar shapes, have exsolved on one side of irregular lattice defects or boundaries, as revealed by band contrast maps (Fig. 9e). Moreover, the thin exsolved Mg-rich pigeonite occurs within the boundary layers between partially melted and deformed host domains at the nanoscale (Figs. 7b and 9d), which coincides with the microscale observations of Mg-rich pigeonite close to fractures or partially melted domains at the rim of host pyroxene (Figs. 1c–1d). These exsolution phenomena are different from the lamellar exsolution behavior observed in martian pyroxene (Leroux et al. 2004; Leroux et al. 2016), suggesting that the exsolved pigeonite in this study could be driven or modified by shock deformations, not be solely related to the slow endogenic cooling processes.

Composition Constraints on the Pigeonite Formation

This single pyroxene grain records the magma evolution of lunar basalts at the CE-5 landing site (trend 1, Figs. 3a–3f). The MgO-rich, Al_2O_3-rich, and TiO_2-rich core of pyroxene (trend 1, Figs. 3e–3f) represents the early-stage pyroxene crystallization near the saturation point of plagioclase and ilmenite in the parent magma (Luo et al. 2023; Wang et al. 2024). As plagioclase and ilmenite began to crystallize, the Al_2O_3 and TiO_2 contents decreased significantly in the magma, which is reflected by the low Al_2O_3 and TiO_2 composition at the pyroxene rim (trend 1, Figs. 1f and 6e–6f).

However, trend 1 slightly deviates from the main pyroxene evolution trend in CE-5 lunar basalts, particularly in its SiO_2, Al_2O_3, and TiO_2 contents (Figs. 3c–3f). Additionally, the shocked pyroxene also exhibits two other evolution trends (trends 2 and 3), which are associated with the pigeonite formation and deviate from the main pyroxene evolution trend in CE-5 lunar basalts, but in the opposite direction relative to trend 1

(Figs. 3c, 3e, and 3f). The co-occurrence of these three trends (trends 1–3), observed in both deformed host and exsolution domains, suggests that exsolution processes modified the original pyroxene composition that crystallized from the parent magma of CE-5 basalts, which has never been reported in pyroxene from CE-5 samples (Wang et al. 2024; Wu et al. 2024).

The direction of element migration (Ca, Mg, and Fe) may differ between endogenic exsolution processes and shock-affected exsolution phenomena in this study. Exsolved augite-pigeonite lamellae typically coarsen bilaterally due to Ca vs. Mg and Fe interdiffusion during slow endogenic cooling (Ross et al. 1970; Putnis 1992; Leroux et al. 2004, 2016; Pittarello et al. 2019), leading to well-defined, straight pigeonite-augite interfaces. Nevertheless, in this study, the bilateral interdiffusion of Ca vs. Mg and Fe is limited within two adjacent boundaries (lattice defects), resulting in the irregular forms of pigeonite-augite interfaces during exsolution (Figs. 9e and 10c). Therefore, these compositional and morphological observations strongly indicate that the exsolution process in this pyroxene is closely linked to shock deformations rather than slow endogenic cooling processes.

Furthermore, EDS maps of the deformed host domains reveal a negative correlation between two distinct elemental groups: Group 1 (Mg, Fe, Si, O) and Group 2 (Ca, Al, Ti; Figs. 1c–1d and 6 and Online Materials[1] Figs. S2–S3). This observed anticorrelation involving the mobility of the O element deviates slightly from the classic pigeonite-augite exsolution mechanism ($Mg^{2+}+Fe^{2+}+2Si^{4+}$ <pigeonite> ↔ $Ca^{2+}+2Al^{3+}+Ti^{4+}$ <augite>, Ross et al. 1970; Putnis 1992; Pittarello et al. 2019). This indicates that in the augite domains, Al may substitute for Si in the T-O tetrahedron of pyroxene, whereas in the exsolution domains, the pigeonite structure is likely dominated by Si-O tetrahedra. The relatively lower O content in augite could also be linked to the transport of Al from pigeonite domains to augite domains, as Al-O tetrahedra can contain much fewer non-bridging or bridging oxygens in glass state compared to Si-O tetrahedra (Dowty 1987). Coincidentally, the Raman anomalies at 822 cm^{-1} triggered by Si–O to Al–O substitution via localized melting and rapid crystallization in most parts of this shocked pyroxene, suggesting that shock deformations and heat from localized melting may facilitate the element diffusion processes within this shocked pyroxene (Figs. 1c–1d and 9d). Elemental distributions at the boundary between impact melt and host pyroxene also indicate pigeonite formation via Ca-Mg interdiffusion (Fig. 9d). This local pigeonite growth points to element partitioning between the melt and pyroxene, confirming an additional mechanism for its formation in shocked pyroxene. Thus, the multiple occurrences of pigeonite within the pyroxene are attributed to both shock-related exsolution affected by plastic deformations and local melt-solid partitioning during frictional melting and cooling processes.

Implications For Shock-Induced Composition Heterogeneity In Pyroxene

Although this single shocked pyroxene reveals distinct compositional heterogeneities, its overall evolution trends align with the composition variations observed in pyroxenes from ~2.0 Ga CE-5 lunar basalts (Figs. 3a–3f, Che et al. 2021; Wang et al. 2024; Wu et al. 2024). This finding suggests that the shocked basaltic clast analyzed in this study is more likely a locally derived, impact-generated fragment from CE-5 lunar basalts rather than an exotic material ejected from distant impact craters. Additionally, the observed shock deformations and frictional melting in this basaltic clast, which indicate a peak shock pressure of 9–17 GPa and a shock duration of ~0.06–2.4 ms, correspond to the impact events forming craters larger than ~30–600 m in diameter (Fig. 10d and Online Materials[1] S9). Based on the remote sensing data and crater ejecta modeling, local craters within 1 km of the CE-5 landing site contributed up to 88% of the ejecta materials (~49 cm in thickness) to the lunar regolith at this location (Jia et al. 2022; Qian et al. 2021a; Qian et al. 2021b). Among these, two impact craters, including Xuguangqi (~400 m in diameter) and C2 (~100 m in diameter), ejected about ~30 and ~12 cm thick deposits, respectively, to the CE-5 landing site (Qian et al. 2021a, 2021b; Jia et al. 2022). The shock metamorphism in this basaltic clast that was drilled at a depth of ~10 cm in the lunar regolith at the CE-5 landing site aligns with remote sensing interpretations, suggesting a local impact origin. The small impact craters (Xuguangqi and C2) may have played a key role in generating the shock metamorphic effects in pyroxene in this study. More broadly, similar shocked clasts may not be rare in CE-5 samples and could also be present in other lunar regolith deposits, causing the broad variations of pyroxene compositions.

Four distinct compositional evolution trends in pyroxene at the microscale correspond to the magmatic crystallization (trend 1, Fig. 3a), shock-related exsolution by deformations (trend 2 and 3, Fig. 3a), and shock-induced melting processes (trend 4, Fig. 3a), respectively. Shock-related exsolution by deformations can potentially redistribute the intra-crystalline compositions in pyroxene. This implies that, in addition to the typical magmatic evolution trend recorded in pyroxene (Fig. 3 and Online Materials[1] Fig. S6, Wang et al. 2024; Wu et al. 2024), the complex and broad compositional variations in pyroxene from CE-5 samples (Figs. 3a–3f) likely result from the local impact processes. Additionally, pyroxene recrystallized from the shock-melted materials contains high contents of FeO, CaO, Al_2O_3, and TiO_2 due to the incorporation of melted ilmenite, plagioclase, and Fe-rich pyroxene (trend 4, Figs. 3e–3f), which may explain the presence of composition outliers with high Al_2O_3 and TiO_2 contents from previous data (Figs. 3e–3f). Furthermore, the partitioning processes between impact melt and host pyroxene modify the composition variations at the nanoscale (Fig. 9d). Therefore, compositional data obtained without detailed microstructural analysis of pyroxene may not solely represent magmatic processes, as shock-induced deformations and melting can influence the major element composition (and possibly even the trace elements) in pyroxene.

IMPLICATIONS

(1) Shock-induced structural modifications in pyroxene, including the dislocation [001](100) glide system, pigeonite exsolutions, and localized frictional melting, are identified in the shocked clast. Concurrently, shock twins and displacements

in ilmenite document shock shearing under low-to-moderate shock conditions.

(2) Raman spectroscopy reveals an anomalous peak at ~822 cm^{-1} within the pyroxene, indicative of Si-Al substitution by localized melting and rapid crystallization, making it a useful indicator for impact events. Shock-induced plastic deformations and localized heating by fractional melting can facilitate the formation of pigeonite or alter the existing exsolved pigeonite in pyroxene.

(3) The observed intra-crystal compositional variations, characterized by four distinct evolution trends, align with the complex patterns reported in magmatic pyroxene systems. However, the localized nature of these variations and their close association with shock microstructures suggest that they are primarily driven by impact-induced processes rather than pristine magmatic fractionation. This finding underscores the necessity of differentiating shock metamorphism from magmatic processes when interpreting pyroxene-based petrogenetic histories.

Acknowledgments and Funding

We thank China National Space Administration (CNAS) for providing the CE-5 sample CE5Z0906YJ. This study was supported by the National Natural Science Foundation of China (grants: 42403039, 42241111, and 42441802), the Postdoctoral Fellowship Program of CPSF (grant: GZB20230680), the China Postdoctoral Science Foundation Funded Project (grants: 2024M763056 and 2025T180114), and the MOST Special Fund from State Key Laboratory of Geological Processes and Mineral Resources, China University of Geosciences (grant: MSFGPMR2024-606), and the Science and Technology Development Fund of Macau (Grant numbers 0052/2024/RIA1). We sincerely appreciate the constructive guidance from two reviewers (Timmons Erickson and Jinping Hu) and the associate editor (Steven Simon).

References Cited

Ashworth, J.R. (1980) Deformation mechanisms in mildly shocked chondritic diopside. Meteoritics, 15, 105–115, https://doi.org/10.1111/j.1945-5100.1980.tb00514.x.

Beck, P., Gillet, P., El Goresy, A., and Mostefaoui, S. (2005) Timescales of shock processes in chondritic and martian meteorites. Nature, 435(7045), 1071–1074, https://doi.org/10.1038/nature03616.

Bence, A., and Papike, J. (1972) Pyroxenes as recorders of lunar basalt petrogenesis: Chemical trends due to crystal-liquid interaction. Proceedings of the Lunar Science Conference, p. 431.

Cao, H., Wang, C., Chen, J., Che, X., Fu, X., Shi, Y., Liu, D., Ling, Z., Qiao, L., Lu, X., Qi, X., Yin, C., Liu, P., Liu, C., Xin, Y., and Liu, J. (2022. A Raman Spectroscopic and Microimage Analysis Perspective of the Chang'e-5 Lunar Samples. Geophysical Research Letters, 49(13), e2022GL099282, https://doi.org/10.1029/2022GL099282.

Cardwell, R.K., Chinn, D.S., Moore, G.F., and Turcotte, D.L. (1978) Frictional heating on a fault zone with finite thickness. Geophysical Journal International, 52, 525–530, https://doi.org/10.1111/j.1365-246X.1978.tb04247.x

Che, X., Nemchin, A., Liu, D., Long, T., Wang, C., Norman, M.D., Joy, K.H., Tartese, R., Head, J., Jolliff, B., and others. (2021) Age and composition of young basalts on the Moon, measured from samples returned by Chang'e-5. Science, 374, 887–890, https://doi.org/10.1126/science.abl7957.

Daly, L., Lee, M.R., Piazolo, S., Griffin, S., Bazargan, M., Campanale, F., Chung, P., Cohen, B.E., Pickersgill, A.E., Hallis, L.J., and others. (2019) Boom boom pow: Shock-facilitated aqueous alteration and evidence for two shock events in the Martian nakhlite meteorites. Science Advances, 5, eaaw5549, https://doi.org/10.1126/sciadv.aaw5549.

Dellefant, F., Trepmann, C.A., Gilder, S.A., Sleptsova, I.V., Kaliwoda, M., and Weiss, B.P. (2022) Ilmenite and magnetite microfabrics in shocked gneisses from the Vredefort impact structure, South Africa. Contributions to Mineralogy and Petrology, 177, 88, https://doi.org/10.1007/s00410-022-01950-5.

Dowty, E. (1987) Vibrational interactions of tetrahedra in silicate glasses and crystals: II. Calculations on melities, pyroxenes, silica polymorphs and feldspars. Physics and Chemistry of Minerals, 14, 122–138, https://doi.org/10.1007/BF00308216.

Feng, L., Miyahara, M., Nagase, T., Ohtani, E., Hu, S., El Goresy, A., and Lin, Y. (2017) Shock-induced *P-T* conditions and formation mechanism of akimotoite-pyroxene glass assemblages in the Grove Mountains (GRV) 052082 (L6) meteorite. American Mineralogist, 102, 1254–1262, https://doi.org/10.2138/am-2017-5905.

Filiberto, J., Gross, J., Udry, A., Trela, J., Wittmann, A., Cannon, K.M., Penniston-Dorland, S., Ash, R., Hamilton, V.E., Meado, A.L., and others. (2018) Shergottite Northwest Africa 6963: A Pyroxene-Cumulate Martian Gabbro. Journal of Geophysical Research. Planets, 123, 1823–1841, https://doi.org/10.1029/2018JE005635.

Fleet, S., Chandrasekhar, S., and Megaw, H. (1966) The structure of bytownite ('body-centred anorthite'). Acta Crystallographica, 21, 782–801, https://doi.org/10.1107/S0365110X66003840.

Fritz, J., Artemieva, N., and Greshake, A. (2005) Ejection of Martian meteorites. Meteoritics & Planetary Science, 40, 1393–1411, https://doi.org/10.1111/j.1945-5100.2005.tb00409.x.

Fritz, J., Greshake, A., and Fernandes, V.A. (2017) Revising the shock classification of meteorites. Meteoritics & Planetary Science, 52, 1216–1232, https://doi.org/10.1111/maps.12845.

Grove, T.L. (1982) Use of exsolution lamellae in lunar clinopyroxenes as cooling rate speedometers: An experimental calibration. American Mineralogist, 67, 251–268.

Harrison, R.J., Redfern, S.A.T., and Smith, R.I. (2000) In-situ study of the $R\bar{3}$ to $R\bar{3}c$ phase transition in the ilmenite-hematite solid solution using time-of-flight neutron powder diffraction. American Mineralogist, 85, 194–205, https://doi.org/10.2138/am-2000-0119.

He, Q., Li, Y., Baziotis, I., Qian, Y., Xiao, L., Wang, Z., Zhang, W., Luo, B., Neal, C.R., Day, J.M.D., and others. (2022) Detailed petrogenesis of the unsampled *Oceanus Procellarum*: The case of the Chang'e-5 mare basalts. Icarus, 383, 115082, https://doi.org/10.1016/j.icarus.2022.115082.

Henry, H., Tilhac, R., Griffin, W.L., O'Reilly, S.Y., Satsukawa, T., Kaczmarek, M.-A., Grégoire, M., and Ceuleneer, G. (2017) Deformation of mantle pyroxenites provides clues to geodynamic processes in subduction zones: Case study of the Cabo Ortegal Complex, Spain. Earth and Planetary Science Letters, 472, 174–185, https://doi.org/10.1016/j.epsl.2017.05.028.

Hu, J., Asimow, P.D., Liu, Y., and Ma, C. (2023) Shock-recovered maskelynite indicates low-pressure ejection of shergottites from Mars. Science Advances, 9, eadf2906, https://doi.org/10.1126/sciadv.adf2906.

Huang, E., Chen, C.H., Huang, T., Lin, E.H., and Xu, J. (2000) Raman spectroscopic characteristics of Mg-Fe-Ca pyroxenes. American Mineralogist, 85, 473–479, https://doi.org/10.2138/am-2000-0408.

Imae, N. and Ikeda, Y. (2010) High-pressure polymorphs of magnesian orthopyroxene from a shock vein in the Yamato-000047 lherzolitic shergottite. Meteoritics & Planetary Science, 45, 43–54, https://doi.org/10.1111/j.1945-5100.2009.01004.x.

Jia, B., Fa, W., Zhang, M., Di, K., Xie, M., Tai, Y., and Li, Y. (2022) On the provenance of the Chang'E-5 lunar samples. Earth and Planetary Science Letters, 596, 117791, https://doi.org/10.1016/j.epsl.2022.117791.

Jin, Z., Hou, T., Zhu, M.-H., Zhang, Y., and Namur, O. (2024) Late-stage microstructures in Chang'E-5 basalt and implications for the evolution of lunar ferrobasalt. American Mineralogist, 110, 560–569, doi:https://doi.org/10.2138/am-2024-9448.

Kirby, S.H. and Christie, J.M. (1977) Mechanical twinning in diopside Ca(Mg,Fe) Si_2O_6: Structural mechanism and associated crystal defects. Physics and Chemistry of Minerals, 1, 137–163, https://doi.org/10.1007/BF00307315.

Kirby, S.H. and Etheridge, M.A. (1981) Exsolution of Ca-clinopyroxene from orthopyroxene aided by deformation. Physics and Chemistry of Minerals, 7, 105–109, https://doi.org/10.1007/BF00308225.

Koeberl, C., and Henkel, H. (2005) Impact Tectonics, p. 1–80. Springer.

Langenhorst, F. and Poirier, J.-P. (2000) Anatomy of black veins in Zagami: Clues to the formation of high-pressure phases. Earth and Planetary Science Letters, 184, 37–55, https://doi.org/10.1016/S0012-821X(00)00317-4.

Langenhorst, F., Joreau, P., and Doukhan, J.C. (1995) Thermal and shock metamorphism of the Tenham chondrite: A TEM examination. Geochimica et Cosmochimica Acta, 59, 1835–1845, https://doi.org/10.1016/0016-7037(95)00086-F.

Leroux, H. (2001) Microstructural shock signatures of major minerals in meteorites. European Journal of Mineralogy, 13, 253–272, https://doi.org/10.1127/0935-1221/01/0013-0253.

Leroux, H., Doukhan, J.C., and Langenhorst, F. (1994) Microstructural defects in experimentally shocked diopside: A TEM characterization. Physics and Chemistry of Minerals, 20, 521–530, https://doi.org/10.1007/BF00211847.

Leroux, H., Devouard, B., Cordier, P., and Guyot, F. (2004) Pyroxene microstructure in the Northwest Africa 856 martian meteorite. Meteoritics & Planetary Science, 39, 711–722, https://doi.org/10.1111/j.1945-5100.2004.tb00114.x.

Leroux, H., Jacob, D., Marinova, M., Hewins, R.H., Zanda, B., Pont, S., Lorand, J.-P., and Humayun, M. (2016) Exsolution and shock microstructures of igneous pyroxene clasts in the Northwest Africa 7533 Martian meteorite. Meteoritics & Planetary Science, 51, 932–945, https://doi.org/10.1111/maps.12637.

Lindsley, D.H. and Andersen, D.J. (1983) A two-pyroxene thermometer. Journal of Geophysical Research: Solid Earth, 88 (S02), A887–A906, https://doi.org/10.1029/JB088iS02p0A887.

Liu, X.-W., Jin, Z.-M., and Green, H.W. II. (2007) Clinoenstatite exsolution in diopsidic augite of Dabieshan: Garnet peridotite from depth of 300 km. American Mineralogist, 92, 546–552, https://doi.org/10.2138/am.2007.2232.

Long, T., Qian, Y., Norman, M.D., Miljkovic, K., Crow, C., Head, J.W., Che, X., Tartèse, R., Zellner, N., Yu, X., and others. (2022) Constraining the formation and transport of lunar impact glasses using the ages and chemical compositions of Chang'e-5 glass beads. Science Advances, 8, eabq2542, https://doi.org/10.1126/sciadv.abq2542.

Luo, B., Wang, Z., Song, J., Qian, Y., He, Q., Li, Y., Head, J.W., Moynier, F., Xiao, L., Becker, H., and others. (2023) The magmatic architecture and evolution of the Chang'e-5 lunar basalts. Nature Geoscience, 16, 301–308, https://doi.org/10.1038/s41561-023-01146-x.

Minkin, J. A., and Chao, E. (1971) Single crystal X-ray investigation of deformation in terrestrial and lunar ilmenite. Lunar and Planetary Science Conference Proceedings, 2, 237–246

Miyamoto, M. and Takeda, H. (1977) Evaluation of a crust model of eucrites from the width of exsolved pyroxene. Geochemical Journal, 11, 161–169, https://doi.org/10.2343/geochemj.11.161.

Miyamoto, M., Mikouchi, T., and Kaneda, K. (2001) Thermal history of the Ibitira noncumulate eucrite as inferred from pyroxene exsolution lamella: Evidence for reheating and rapid cooling. Meteoritics & Planetary Science, 36, 231–237, https://doi.org/10.1111/j.1945-5100.2001.tb01867.x.

Mollo, S., Del Gaudio, P., Ventura, G., Iezzi, G., and Scarlato, P. (2010) Dependence of clinopyroxene composition on cooling rate in basaltic magmas: Implications for thermobarometry. Lithos, 118, 302–312, https://doi.org/10.1016/j.lithos.2010.05.006.

Mori, H. and Takeda, H. (1981) Thermal and deformational histories of diogenites as inferred from their microtextures of orthopyroxene. Earth and Planetary Science Letters, 53, 266–274, https://doi.org/10.1016/0012-821X(81)90159-X.

Müller, W.F. (1993) Thermal and deformation history of the Shergotty meteorite deduced from clinopyroxene microstructure. Geochimica et Cosmochimica Acta, 57, 4311–4322, https://doi.org/10.1016/0016-7037(93)90325-Q.

Pang, R., Yang, J., Du, W., Zhang, A., Liu, S., and Li, R. (2022) New occurrence of seifertite and stishovite in Chang'E-5 regolith. Geophysical Research Letters, 49(12), e2022GL098722, doi:https://doi.org/10.1029/2022GL098722.

Papike, J.J., Ryder, G., and Shearer, C.K. (1998) Lunar samples. In J.J. Papike, Ed., Planetary Materials, Chapter 5, p. 719–952. Reviews in Mineralogy, 36, Mineralogical Society of America.

Papike, J.J., Karner, J.M., and Shearer, C.K. (2005) Comparative planetary mineralogy: Valence state partitioning of Cr, Fe, Ti, and V among crystallographic sites in olivine, pyroxene, and spinel from planetary basalts. American Mineralogist, 90, 277–290, https://doi.org/10.2138/am.2005.1779.

Pernet-Fisher, J.F., Howarth, G.H., Liu, Y., Chen, Y., and Taylor, L.A. (2014) Estimating the lunar mantle water budget from phosphates: Complications associated with silicate-liquid-immiscibility. Geochimica et Cosmochimica Acta, 144, 326–341, https://doi.org/10.1016/j.gca.2014.09.004.

Pittarello, L., McKibbin, S., Yamaguchi, A., Ji, G., Schryvers, D., Debaille, V., and Claeys, P. (2019) Two generations of exsolution lamellae in pyroxene from Asuka 09545: Clues to the thermal evolution of silicates in mesosiderite. American Mineralogist, 104, 1663–1672, https://doi.org/10.2138/am-2019-7001.

Presnall, D.C. and Gasparik, T. (1990) Melting of enstatite ($MgSiO_3$) from 10 to 16.5 GPa and the forsterite (Mg_2SiO_4)-majorite ($MgSiO_3$) eutectic at 16.5 GPa: Implications for the origin of the mantle. Journal of Geophysical Research: Solid Earth, 95 (B10), 15771–15777, https://doi.org/10.1029/JB095iB10p15771.

Putnis, A. (1992) Transformation processes in minerals I: exsolution. In A. Putnis, Ed., An Introduction to Mineral Sciences, p. 333–386. Cambridge University Press.

Qian, Y., Xiao, L., Head, J. W., Wöhler, C., Bugiolacchi, R., Wilhelm, T., Althoff, S., Ye, B., He, Q., Yuan, Y., and Zhao, S. (2021a) Copernican-Aged (<200 Ma) Impact Ejecta at the Chang'e-5 Landing Site: Statistical Evidence From Crater Morphology, Morphometry, and Degradation Models. Geophysical Research Letters, 48(20), e2021GL095341, https://doi.org/10.1029/2021GL095341.

Qian, Y., Xiao, L., Wang, Q., Head, J.W., Yang, R., Kang, Y., van der Bogert, C.H., Hiesinger, H., Lai, X., Wang, G., and others. (2021b) China's Chang'e-5 landing site: Geology, stratigraphy, and provenance of materials. Earth and Planetary Science Letters, 561, 116855, https://doi.org/10.1016/j.epsl.2021.116855.

Reddy, S.M., Timms, N.E., Pantleon, W., and Trimby, P. (2007) Quantitative characterization of plastic deformation of zircon and geological implications. Contributions to Mineralogy and Petrology, 153, 625–645, https://doi.org/10.1007/s00410-006-0174-4.

Ringwood, A.E. and Major, A. (1966) High-pressure transformations in pyroxenes. Earth and Planetary Science Letters, 1, 351–357, https://doi.org/10.1016/0012-821X(66)90023-9.

Ross, M., Bence, A., Dwornik, E., Clark, J.R., and Papike, J. (1970) Mineralogy of the lunar clinopyroxenes, augite and pigeonite. Geochimica et Cosmochimica Acta, 1, 839–840.

Salviulo, G., Secco, L., Antonini, P., and Piccirillo, E.M. (1997) *C*2/*c* pyroxene from two alkaline sodic suites (Western Ross Embayment; Antarctica); crystal chemical characterization and its petrologic significance. Mineralogical Magazine, 61, 423–439, https://doi.org/10.1180/minmag.1997.061.406.08.

Saxena, S.K., Ghose, S., and Turnock, A.C. (1974) Cation distribution in low-calcium pyroxenes: Dependence on temperature and calcium content and the thermal history of lunar and terrestrial pigeonites. Earth and Planetary Science Letters, 21, 194–200, https://doi.org/10.1016/0012-821X(74)90054-5.

Schaal, R.B., and Hörz, F. (1977) Shock metamorphism of lunar and terrestrial basalts. Proceedings of the 8th Lunar Science Conference, p. 1697–1729, Houston, Texas.

Sharma, S.K., Simons, B., and Yoder, H.S. (1983) Raman study of anorthite, calcium Tschermak's pyroxene, and gehlenite in crystalline and glassy states. American Mineralogist, 68, 1113–1125.

Spray, J.G. (2010) Frictional Melting Processes in Planetary Materials: From Hypervelocity Impact to Earthquakes. Annual Review of Earth and Planetary Sciences, 38, 221–254, doi:https://doi.org/10.1146/annurev.earth.031208.100045.

Stöffler, D., Ostertag, R., Jammes, C., Pfannschmidt, G., Gupta, P.R.S., Simon, S.B., Papike, J.J., and Beauchamp, R.H. (1986) Shock metamorphism and petrography of the Shergotty achondrite. Geochimica et Cosmochimica Acta, 50, 889–903, https://doi.org/10.1016/0016-7037(86)90371-6.

Stöffler, D., Hamann, C., and Metzler, K. (2018) Shock metamorphism of planetary silicate rocks and sediments: Proposal for an updated classification system. Meteoritics & Planetary Science, 53, 5–49, https://doi.org/10.1111/maps.12912.

Takeda, H., Miyamoto, M., Ishii, T., and Lofgren, G.E. (1975) Relative cooling rates of mare basalts at the Apollo 12 and 15 sites as estimated from pyroxene exsolution data. Proceedings of the Sixth Lunar Science Conference, p. 987–996, Houston, Texas.

Takeda, H., Mori, H., Ishii, T., and Miyamoto, M. (1982) Thermal and impact histories of pyroxenes in lunar eucrite-like gabbros and eucrites. Lunar and Planetary Science Conference, p. 1297–1313, Houston, Texas.

Tian, H.C., Wang, H., Chen, Y., Yang, W., Zhou, Q., Zhang, C., Lin, H.L., Huang, C., Wu, S.T., Jia, L.H., and others. (2021) Non-KREEP origin for Chang'e-5 basalts in the Procellarum KREEP Terrane. Nature, 600, 59–63, https://doi.org/10.1038/s41586-021-04119-5.

Veksler, I.V., Dorfman, A.M., Borisov, A.A., Wirth, R., and Dingwell, D.B. (2007) Liquid Immiscibility and the Evolution of Basaltic Magma. Journal of Petrology, 48, 2187–2210, https://doi.org/10.1093/petrology/egm056.

Veksler, I.V., Dorfman, A.M., Rhede, D., Wirth, R., Borisov, A.A., and Dingwell, D.B. (2008) Liquid unmixing kinetics and the extent of immiscibility in the system K_2O–CaO–FeO–Al_2O_3–SiO_2. Chemical Geology, 256, 119–130, https://doi.org/10.1016/j.chemgeo.2008.06.033.

von Engelhardt, W., Arndt, J., Müller, W.F., and Stöffler, D. (1970) Shock metamorphism in lunar samples. Science, 167, 669–670, https://doi.org/10.1126/science.167.3918.669.

Walton, E.L., Sharp, T.G., and Hu, J. (2016) Frictional melting processes and the generation of shock veins in terrestrial impact structures: Evidence from the Steen River impact structure, Alberta, Canada. Geochimica et Cosmochimica Acta, 180, 256–270, https://doi.org/10.1016/j.gca.2016.02.024.

Wang, A., Jolliff, B.L., Haskin, L.A., Kuebler, K.E., and Viskupic, K.M. (2001) Characterization and comparison of structural and compositional features of planetary quadrilateral pyroxenes by Raman spectroscopy. American Mineralogist, 86, 790–806, https://doi.org/10.2138/am-2001-0703.

Wang, C., Xu, Y.-G., Zhang, L., Chen, Z., Xia, X., Lin, M., and Guo, F. (2024) A shallow (<100 km) ilmenite-bearing pyroxenitic source for young lunar volcanism. Earth and Planetary Science Letters, 639, 118770, https://doi.org/10.1016/j.epsl.2024.118770.

Wu, Y., Liao, S., Yan, P., Xiao, Z., Yin, Z., Yang, W., Wang, H., Tian, H., Hui, H., Pan, L., and others. (2023) Impact-related chemical modifications of the Chang'E-5 lunar regolith. Geochimica et Cosmochimica Acta, 363, 94–113, https://doi.org/10.1016/j.gca.2023.10.031.

Wu, F., Li, Q., Chen, Y., Hu, S., Yue, Z., Zhou, Q., Wang, H., Yang, W., Tian, H., Zhang, C., and others. (2024) Lunar evolution in light of the Chang'e-5 returned samples. Annual Review of Earth and Planetary Sciences, 52, 159–194, https://doi.org/10.1146/annurev-earth-040722-100453.

Zhang, A., Hsu, W., Wang, R., and Ding, M. (2006) Pyroxene polymorphs in melt veins of the heavily shocked Sixiangkou L6 chondrite. European Journal of Mineralogy, 18, 719–726, https://doi.org/10.1127/0935-1221/2006/0018-0719.

Zhao, S., Zhang, G., Sun, H., Mason, R., and He, X. (2017) Orientation of exsolution lamellae in mantle xenolith pyroxenes and implications for calculating exsolution pressures. American Mineralogist, 102, 2096–2105, https://doi.org/10.2138/am-2017-6009.

Manuscript received April 24, 2025
Manuscript accepted September 25, 2025
Accepted manuscript online October 3, 2025
Manuscript Handled by Steven Simon

Endnotes:

[1] Deposit item AM-26-39877. Online Materials are free to all readers. Go online, via the table of contents or article view, and find the tab or link for supplemental materials.